D-β-hydroxybutyrate stabilizes hippocampal CA3-CA1 circuit during acute insulin resistance.

Bartosz Kula[1], Botond Antal[2,3], Corey Weistuch[4], Florian Gackière[5], Alexander Barre[5], Victor Velado[6], Jeffrey M Hubbard[5], Maria Kukley[7,8], Lilianne R Mujica-Parodi[2,3,9,*], and Nathan A Smith[1,6,10,*].

1 Del Monte Institute for Neuroscience, Department of Neuroscience, University of Rochester, School of Medicine and Dentistry, Rochester, USA

2 Department of Biomedical Engineering, Stony Brook University, Stony Brook, USA

3 Athinoula A. Martinos Center for Biomedical Imaging, Massachusetts General Hospital and Harvard Medical School, Boston, USA

4 Department of Medical Physics, Memorial Sloan Kettering Cancer Center, New York, NY, USA

5 Neuroservices Alliance, Les Jardins de l'Entreprise, Quartier de le Confrérie, Le Puy Ste Réparade, France

6 Center for Neuroscience Research, Children's National Research Institute, Children's National Hospital, Washington D.C., USA

7 Achucarro Basque Center for Neuroscience, Leioa, Spain

8 Ikerbasque - Basque Foundation for Science, Bilbao, Spain

9 Laufer Center for Physical and Quantitative Biology, Stony Brook University, Stony Brook, USA

10 George Washington University School of Medicine and Health Sciences, Washington D.C., USA

* Corresponding authors: lilianne.strey@stonybrook.edu (LMP);
Nathan_Smith@urmc.rochester.edu (NAS)

1. **Abstract**

The brain primarily relies on glycolysis for mitochondrial respiration but switches to alternative fuels such as ketone bodies (KB) during low glucose availability. Neuronal KB uptake, which does not rely on the glucose transporter 4 (GLUT4) and insulin, has shown promising clinical

applications in alleviating the neurological and cognitive effects of disorders with hypometabolic components. However, the specific mechanisms by which such interventions affect neuronal functions are poorly understood. In this study, we pharmacologically blocked GLUT4 to investigate the effects of the exogenous KB D-β-hydroxybutyrate (D-βHb) on mouse brain metabolism during acute insulin resistance (AIR). We found the impact of D-βHb to be distinct across neuronal compartments: AIR decreased synaptic activity and LTP, and impaired axonal conduction, synchronization, and action potential (AP) properties. D-βHb rescued neuronal functions associated with axonal conduction, synchronization and LTP.

Keywords: hippocampus, ketone bodies, beta-hydroxybutyrate, ketogenic diet, insulin resistance, GLUT4, hypometabolism, Schaffer collaterals, pyramidal neurons

2. **Introduction**

Over the past two decades, research on insulin signaling in the brain has become increasingly important in the contexts of type 2 diabetes mellitus (T2DM) and Alzheimer's disease (AD) [1,2]. Insulin plays a critical role in memory formation processes in the hippocampus, such that systemic insulin resistance can interfere with hippocampal metabolism and cognitive function, as shown by various studies [3,4]. Additionally, insulin is an essential element in memory processing in the hippocampus and a vital mediator of cognitive impairments in T2DM and AD, due to its function in promoting GLUT4 translocation [5,6]. Although insulin from the blood crosses the blood-brain barrier, research suggests supplementary local insulin synthesis and release in the brain [7] which enhances the pro-cognitive effects of brain glucose [8]. Therefore, impaired glucose uptake in the hippocampus may contribute to cognitive decline associated with aging, T2DM, and AD [9,10,11].

This relationship has led to the hypothesis that brain hypometabolism reflects encroaching neuronal insulin resistance. The hippocampus is highly enriched with the GLUT4 receptor, which is the primary neuronal insulin dependent glucose transporter, particularly in brain areas with high concentrations of insulin receptors and relatively high neuronal activity [8,12,13]. Insulin acts by enhancing GLUT4 translocation across neuronal membranes under regulation of phosphatidylinositol 3-kinase (PI3K), which furthermore promotes memory formation [14,15]. During memory formation, GLUT4 is primarily expressed in the soma rather than in the more metabolically active hippocampal neuropil [16,17], suggesting that insulin effects may be primarily involved in maintenance of neuronal firing. Mouse models of AD or diet-induced obesity (DIO) showed blunting of the pro-cognitive effects of intrahippocampal insulin injections, along with decreased local glucose metabolism [18,19], coupled with neuronal hyperexcitability with epileptiform spikes and impairment of GLUT4 translocation [20].

During periods of lower glucose availability, ketone bodies (KBs) are supplementing metabolism

as an alternative fuel [21,22]. Introduction of a ketogenic diet has shown pro-cognitive benefits in patients suffering from T2DM or AD. These benefits may arise from a reduction in neuronal firing rates during ketosis [23,24], increased ATP:ADP ratios [25], increased secretion of GABA due to substantial formation of acetyl-CoA [26], equilibration of the NAD:NADH, and curtailed production of free radicals, observed during ketogenic diet, together may help to temper neuronal hyperexcitability and its metabolic consequences [27,28].

In addition, KBs play a crucial role in protecting mitochondria from acute metabolic stress by preventing mitochondrial permeability transition (mPT) through their effects on intracellular calcium levels [29,30]. Furthermore, KBs can affect neuronal firing by promoting the opening of ATP sensitive K^+ channels (K-ATP), thus reducing the cytosolic pool of ATP generated from glycolysis [24,30].

Exogenous KBs, such as *D*-β-hydroxy-butyrate (DβHb) ester, unlike a ketogenic diet, can raise KB levels in circulation without severe dietary restrictions [31,32]. It is unclear whether administration of exogenous KBs in the presence of normal plasma glucose levels maintains their neuroprotective effects, but recent studies show that DβHb provided to healthy adults increased their overall brain activity and stabilized functional networks [33,34].

Those observations led us to hypothesize that exogenous KB could be utilized to rescue neuronal metabolism during cerebral insulin resistance. To test these hypotheses, we first established a murine hippocampal model of acute insulin resistance (AIR) through the inhibition of GLUT4 by administration of Indinavir [35,36]. We then studied how neuron-specific insulin resistance affected hippocampal neurons in the CA3-CA1 circuit; a model circuit for studying learning and memory. We tested the effects of D-βHb during AIR to establish the therapeutic potential of exogenous KBs in hypoglycemic animals. In expectation of circuit-wide effects on synaptic and axonal function, we obtained field potential recordings in hippocampus of the treated mice and made patch-clamp recordings in hippocampal slices to assess the in vitro effects of AIR and D-βHb on the electrophysiological properties of CA1 pyramidal neurons and CA1 fast-spiking interneurons (FSI). Finally, we used computational modeling to establish a bridge between our electrophysiological results and the dysfunction of Na^+/K^+ ATPase, as the potential reason for the detrimental changes observed during AIR.

3. **Results**

Various paradigms of synaptic plasticity associated with learning and memory have been identified in the hippocampus. There is extensive documentation of long-term potentiation (LTP) and long-term depression (LTD), spike-timing-dependent plasticity, and EPSP-spike potentiation in many hippocampal circuits, making the hippocampus a classic system for studying neuroplasticity. Furthermore, the hippocampus's simple cytoarchitecture makes it an ideal model system. In this study, we utilized Indinavir, a potent GLUT4 receptor blocker, to pharmacologically

103 induce AIR in the hippocampal slices Our investigation focused on the stratum radiatum of the
104 CA1, where numerous synapses are formed between Schaffer collaterals (SCO) and the apical
105 dendrites of the pyramidal neurons.

106

107 *3.1 Synaptic activity and LTP, but not fiber volleys (FV), are adversely affected by AIR and are*
108 *not reversed by either 0.1 mM or 1 mM DβHb.*

109 To test synaptic transmission within CA1 under a wide range of energetic demands, we measured
110 the circuit's response under 3 different stimulation paradigms. First, we applied mild physiological
111 stimulation (not imposing high energetic demands [37,38]), consisting of paired stimulation
112 applied at 25 Hz, repeated every 20 s over 30-60 trials [**Fig.1A-F**].

113 During the AIR condition, we observed a strong decrease in fEPSP amplitudes; -39.23 ± 8.72%
114 (1st stimulus) and -38.79 ± 8.93% (2nd stim.) compared to baseline (**Fig. 1A**). There was no
115 recovery of amplitude when D-βHb was applied at low (0.1 mM) (+13.10 ± 6.64% and +14.07 ±
116 6.76%, **Fig. 1A**, p=0.34, p=0.30) or high (1 mM) concentrations [**Fig.1A**, -5.98 ± 6.13% and -5.81
117 ± 6.26%, p=0.88; p=0.56]. There were no effects of either AIR or D-βHb+AIR on PPR [**Fig.1B**,
118 Control: 1.89; AIR: 1.92; 0.1 mM D-βHb+AIR: 2.00; 1 mM D-βHb+AIR: 1.88; p=0.54], suggesting
119 that the facilitation at the synaptic sites remained largely unchanged.

120 When applied over sufficient time, our paired stimulation triggered LTP in the CA1, as evident by
121 a gradual increase in the fEPSP amplitudes [**Fig.1C, top**], but no change in PPR [**Fig.1C,**
122 **bottom**]. Therefore, we compared the magnitude of LTP between the groups by calculating a
123 ratio of EPSP amplitudes during the first 10 min with amplitudes at 40 ± 10 min [**Fig. 1D-F**]. The
124 control condition showed the strongest LTP ratio of 1.53 ± 0.13. LTP induction was almost
125 abolished during AIR [**Fig. 1E**, 1.06 ± 0.06 ratio; -30.66 ± 9.42% reduction vs Control, p=0.018]
126 and 0.1 mM D-βHb did not reverse this effect [**Fig. 1E**, 1.08 ± 0.08, +1.25 ± 6.61% AIR vs. D-
127 βHb+AIR 0.1 mM, p > 0.99], 1 mM D-βHb, however, did [**Fig. 1E**, 1.39 ± 0.10, +21.19 ± 7.64%
128 AIR vs. D-βHb+AIR 1 mM, p=0.044].

129 Moreover, we found no significant effects of either AIR or D-βHb+AIR on the amplitudes of the
130 fiber volleys (FV) [**Fig. 1F**, Control: 1.03 ± 0.08 mV; AIR: 0.89 ± 0.07; D-βHb+AIR 0.1 mM: 0.85 ±
131 0.08; D-βHb+AIR 1 mM: 1.03 ± 0.12; p=0.40]. Next, we tested whether the circuit would behave
132 differently under a stronger stimulation that imposed greater metabolic demands. We stimulated
133 the Schaffer collaterals with 20 pulses applied at 25 Hz, with 20 s breaks between trials. To avoid
134 the onset of LTP from skewing the results, we recorded all train stimulations at least 40 min after
135 the paired stimulation paradigm.

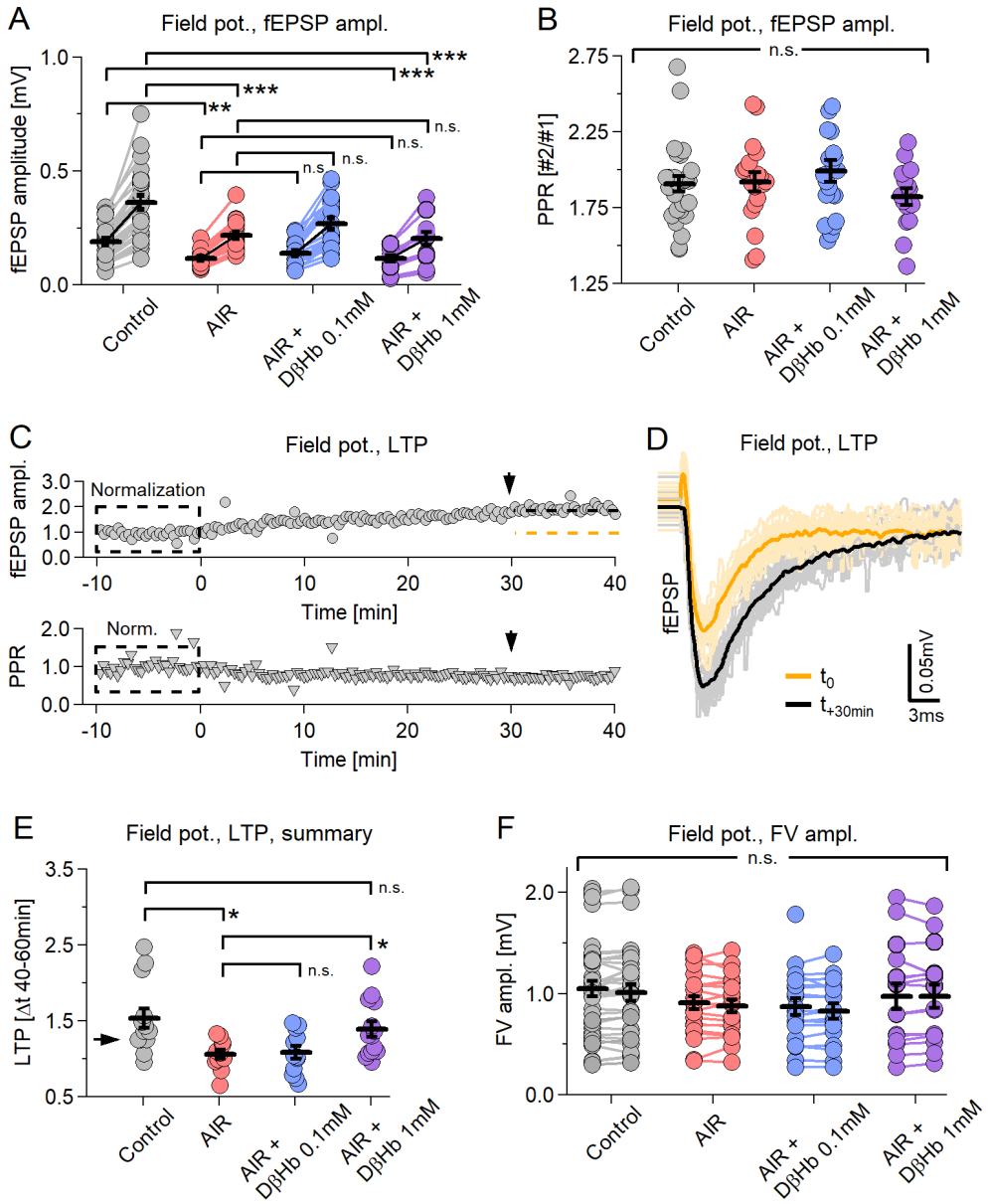

Figure 1: ***Synaptic activity and LTP, but not neuronal firing or PPR, decrease during paired stimulation under AIR, and do not recover during D-βHb administration.***

A) *Scatter plot of the fEPSP amplitudes evoked by paired-pulse stimulation of Schaffer collaterals. Each pair of circles is the average of 30-40 consecutive responses. Black bars represent mean ± SEM. Control fEPSPs in gray, AIR in red; 0.1 mM D-βHb+AIR in blue; 1 mM D-βHb+AIR in purple. Control: n=26 slices; AIR n=19; 0.1 mM D-βHb+AIR: n=20; 1 mM D-βHb+AIR: n=16.* ***B)*** *Scatter plot of the paired-pulse ratio (PPR) of fEPSP recorded in A. The labels, n, are identical to A). No significant differences (p=0.41, ANOVA).* ***C)*** *On top: Representative recording of a Control experiment where paired stimulation was applied for min. Each circle represents fEPSPs amplitude normalized to the average of the first 30 fEPSPs. The dashed orange line represents the mean amplitude at time -10 to 0 min. The black line represents the*

mean amplitude at +30 to +40 min. At the bottom: corresponding normalized PPR. ***D)*** *fEPSPs waveforms recorded in C), showing LTP development. In gray, 30 fEPSP waveforms at t=0 ± 5 min and their average (black). In yellow, 30 fEPSP at time +30 ± 5min and their average (orange). Stimulation artifacts and FVs are removed.* ***E)*** *Scatter plot of LTPs triggered by paired stimulation. Control: n=13; AIR n=11; 0.1 mM D-βHb+AIR: n=12; 1 mM D-βHb+AIR: n=14.* ***F)*** *Scatter plot of the FV amplitudes recorded during A). The labels, n is identical to A). No significant differences (p=0.42, p=0.40; ANOVA). In all plots *p<0.05; **p<0.01; ***p<0.001.*

All compared groups showed potentiation of fEPSP amplitudes during the train, reaching peak at stimuli 5-6. Thereafter, the amplitudes experienced a slight decline but remained potentiated [**Fig. S1A,B**]. Interestingly, throughout the entire stimulation period, the fEPSP amplitudes matched the differences we had seen during paired stimulation [**Fig. S1B**; at stimulus 5: -34.25 ± 11.80% Control vs. AIR, p=0.031; -40.54 ± 11.48% Control vs. 1 mM D-βHb+AIR, p=0.000044; +3.37 ± 7.80 AIR vs. 0.1 mM D-βHb+AIR, p = 0.99; -25.21 ± 7.36% AIR vs. 1 mM D-βHb+AIR, p=0.0054]. The FV amplitudes followed a different pattern, with potentiation at stimulus 2, followed by a consistent decline to approximately 70% of the initial amplitude [**Fig. S1C**]. Similar to paired stimulation, no statistically significant differences were observed between groups at any time point during the train [**Fig. S1C**; p=0.16 to 0.40].

Finally, we examined the hippocampal circuit under conditions of intense non-physiological stimulation. This involved applying long trains of 50 stimuli at 25 Hz, spanning across 60 trials with a 20-second break between each trial. The responses during this specific stimulation varied between trials, making it inappropriate to average them over the entire stimulation period. As a result, we represent the fEPSP and FV amplitudes as heat maps. In these heat maps, each point represents the group's mean response to a single stimulus at a given time point.

Consistent with our previous results, we observed a period of fEPSP amplitude potentiation followed by a steady decline [**Fig. S2A-D**; at maximum, trial 4-6, stimuli 7-9: -34.81 ± 10.56% Control vs. AIR, p=0.0084; -48.27 ± 11.37% Control vs. 1 mM D-βHb+AIR, p=0.00065; +10.19 ± 11.39% AIR vs. 0.1mM D-βHb+AIR, p=0.59; -13.66 ± 9.08% AIR vs. 1mM D-βHb+AIR]. Synaptic depression first emerged during the final stimuli of the trains, roughly 3 min into the stimulation and became more prominent with each subsequent train application [**Fig. S2A-D**]. In general, fEPSP amplitudes of Controls and AIR groups differed substantially through the first 7 min of the recordings [**Fig. S2A**]. Control and 1 mM D-βHb+AIR groups also differed throughout most of the stimulation trains [**Fig. S2B**], but the 0.1 mM D-βHb+AIR and AIR alone groups scarcely differed except at the end of the trains [**Fig. S2C**]. The AIR and 0.1 mM D-βHb group fEPSPs generally remained comparable. FV remained statistically similar between all the groups, with almost the same response pattern [**Fig. S2E-G**], replicating the results from Fig. 1 and Fig. S1.

Taken together, these results strongly suggest that the effects of AIR and/or D-βHb could differ between cellular compartments (i.e., dendritic versus somatic), have different specificity for various cellular compartments, with synapses being particularly susceptible to metabolic challenges induced by GLUT4 inhibition.

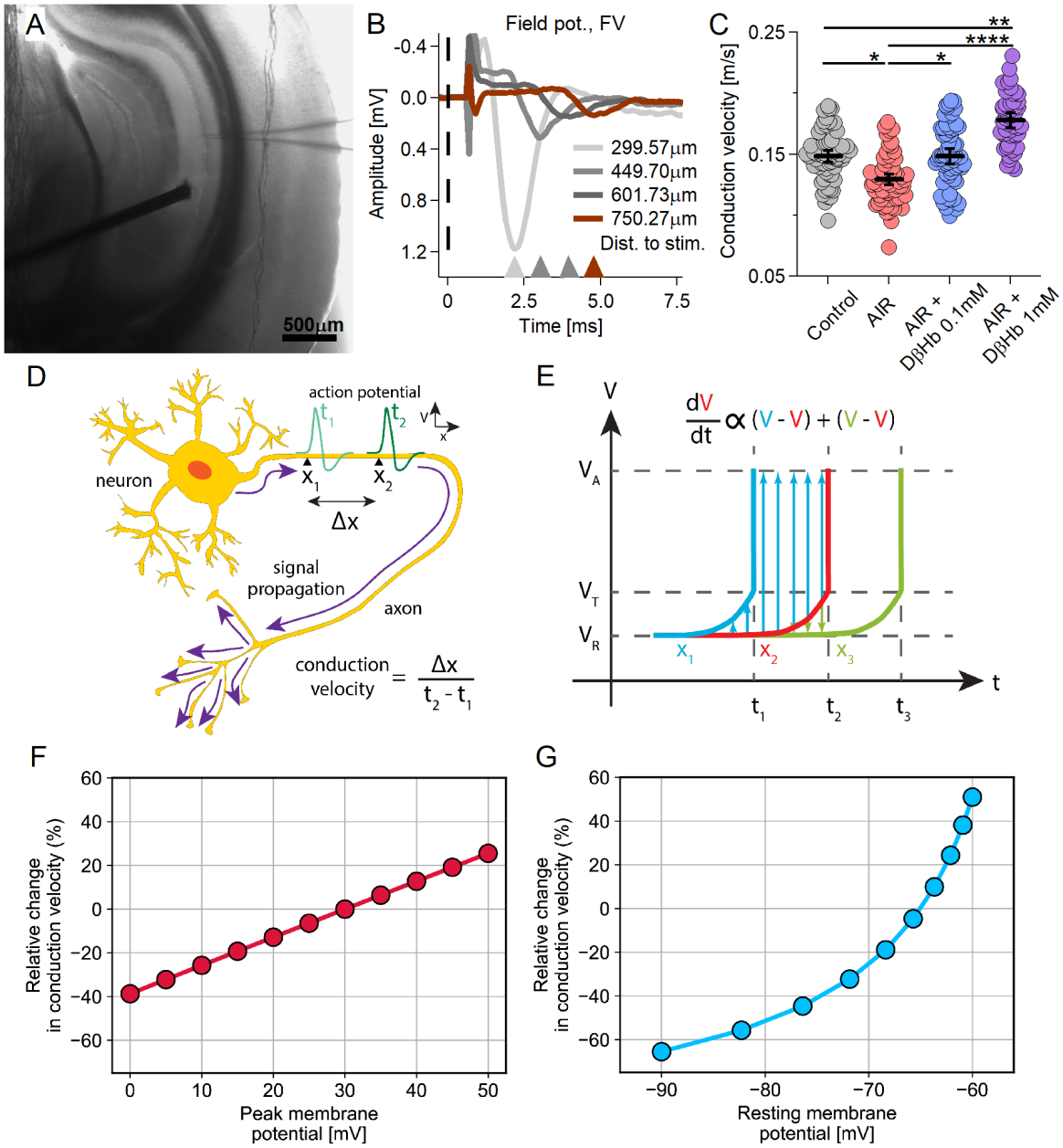

Figure 2: *Conduction velocity (CV) of Schaffer collaterals decreases under AIR are rescued by 0.1 mM D-βHb, and increase with 1mM D-βHb concentration.*

A) *Representative hippocampal slice during CV recording.* ***B)*** *Representative averaged FV waveforms, recorded in CA1. The stimulus onset time (t=0) is marked with a dashed line. Stimulus artifacts are removed.* ***C)*** *Conduction velocity scatter plots. Each colored circle represents a CV replicate. Control in gray, AIR in light red, 0.1 mM D-βHb+AIR in blue, and 1 mM D-βHb+AIR in purple. Data are shown as means ± SEM. *p<0.05; ***p<0.001, nested ANOVA, Control: m=62, n=24, N=14; AIR: m=65, n=22, N=13; 0.1 mM D-βHb+AIR: m=64, n=21, N=13; 1 mM D-βHb+AIR: m=50, n=14, N=10.* ***D)*** *Diagram of conduction velocity of*

an action potential propagating along an axon: distance along the axon (Δx) and the time required for an AP to pass that distance (t_2-t_1). V represents membrane potential. ***E)*** *Model of a propagating action potential. Change in V(t) is shown at a longitudinal increment along the axon (x_2) and at neighboring increments lying immediately ahead (x_1) and behind (x_3). Membrane potential at rest (V_R) changes over time proportionally to the sum of differences between its value and those of the preceding and superseding increments. Upon reaching the threshold potential (V_T), a spike occurs, and the membrane potential reaches peak value (V_A).* ***F-G)*** *CV is modulated by V_A and V_R. Our computational model predicts declining CV due to reductions in the peak of action potentials (F) and/or hyperpolarization of the resting membrane potential (G). CV quantified as percentage, relative to Control.*

3.2 AIR impairs axonal conduction speeds, but D-βHb treatment restores and enhances axonal conduction in a dose-dependent manner.

In the previous sections, we highlighted how AIR and D-βHb affected fEPSPs and FVs, finding a surprising lack of adverse effects of AIR on FV amplitudes, along with a noticeable reduction in fEPSP amplitudes; all further exacerbated by D-βHB. This difference suggests that AIR and/or D-βHb treatment might have differential effects on cellular compartments. We decided to investigate whether any other axonal properties changed during AIR and whether D-βHB remedied such changes.

We found that inducing AIR resulted in a strong reduction in the conduction velocities (CV) of SCOs [**Fig. 2C**; -13.07 ± 2.87% Control vs. AIR, p=0.027]. Addition of 0.1 mM D-βHb during AIR recovered CV back to Control levels [**Fig. 2C**; +12.43 ± 4.42% AIR vs. 0.1 mM D-βHb+AIR, p=0.034; +0.01 ± 0.07% Control vs. 0.1mM D-βHb+AIR, p=0.99] and 1 mM D-βHb significantly improved CV, surpassing the Control [**Fig. 2C**; +31.79 ± 4.59% for AIR vs. 1 mM D-βHb+AIR, p=4.2E-8; +19.10 ± 4.53% for Control vs. 1 mM D-βHb+AIR, p=0.00057].

To enable a better interpretation of these findings, we constructed a computational model of CV by employing an approximation of axonal cable theory (see Methods). Our model examined three processes that determine CV: resting membrane potential (V_R), peak membrane potential (V_A, the amplitude of AP overshoot), and activation threshold potential (V_T, potential for Na_v activation). We considered V_T to be robust to various physiological conditions, given that it primarily depends on Na_v channel type and gating kinetics [39]; therefore, we fixed V_T at a constant value of -50 mV in our calculations. We varied V_R between -90 and -60 mV and V_A between 10 and 30 mV, both of which are considered physiological ranges. We normalized the results to a reference state where V_R = -75 mV, V_A = 30 mV, and V_T = -50 mV. Modeling showed that a decrease in CV required either hyperpolarized resting membrane potential or decreased peak AP amplitude [**Fig. 2F-G**].

3.3 AIR adversely affects input timing, restored by high D-βHb concentrations.

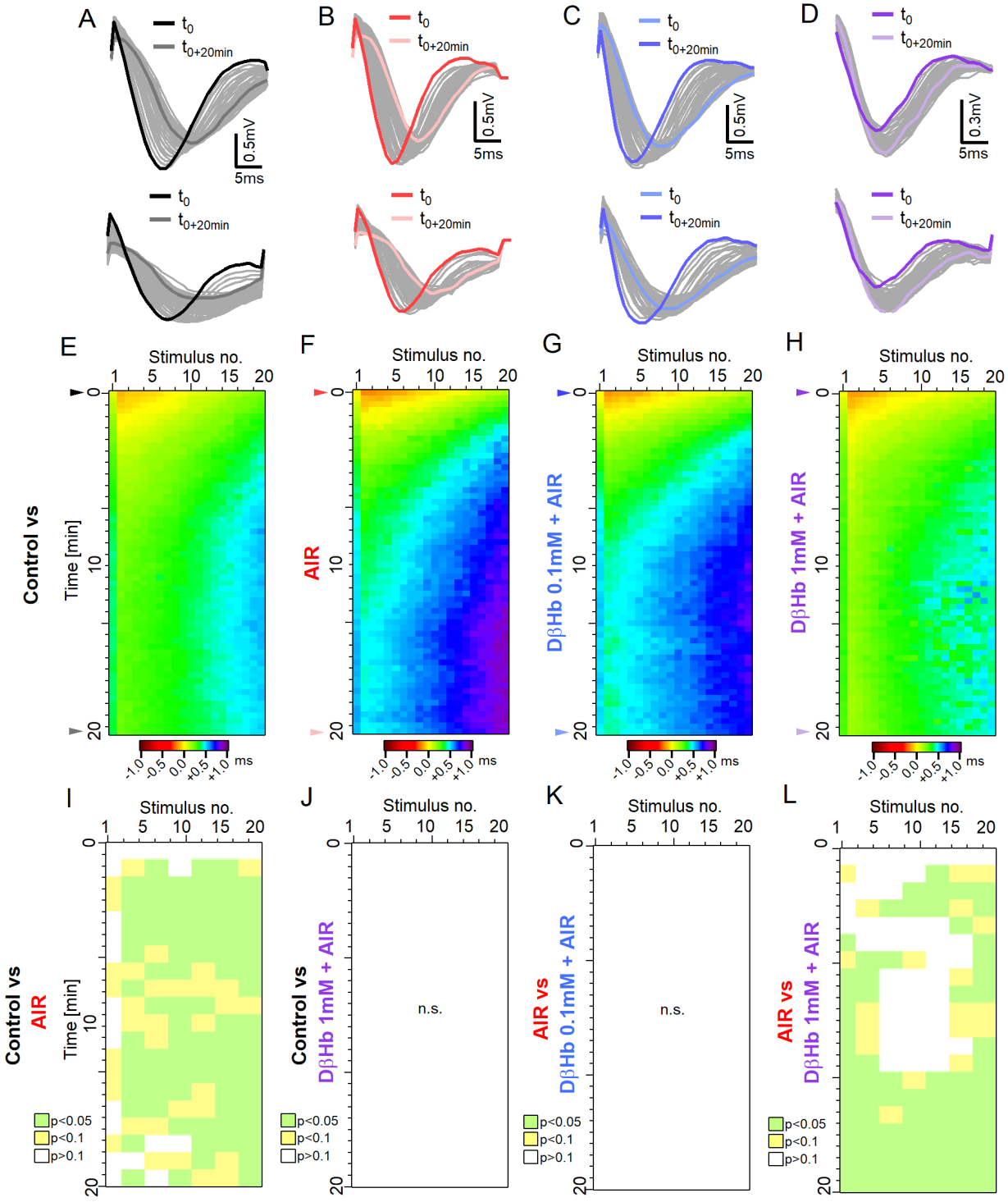

230 **Figure 3:** ***Time delays in axonal firing during train stimulation are increased during AIR and***
231 ***are reversed by 1 mM DβHb.***

232 ***A)*** *Top: Representative example of the FVs recorded at the first stimulus in the control group during*
233 *stimulation with 20 pulses applied at 25 Hz every 20 s, over 20 min. Bottom: FVs recorded in response to*
234 *the last stimulus in each train. The FVs recorded at t = 0 are marked in black; the FVs recorded at t = +20*
235 *min, are marked in dark gray.* ***B) - D)*** *The same as A) in the AIR, 0.1 mM D-βHb+AIR and 1 mM D-βHb+AIR*
236 *groups.* ***E)*** *Heat map of the mean, normalized FV peak latencies recorded in the Control group. Each trial*
237 *is represented by a new row. The columns represent the time points of successive stimuli. Normalized*
238 *latencies (0 ms) are color-coded in yellow. Delays (>0 ms) are color-coded in green-violet, and latency*
239 *improvements (<0 ms) are coded in orange-brown. n=24, N=22.* ***F) - H)*** *The same as E) for AIR, n=16,*
240 *N=15; 0.1 mM D-βHb+AIR. n=17, N=15, 1 mM D-βHb+AIR. n=14, N=10.* ***I)*** *Statistical comparison of*
241 *latencies for the Control (E) and AIR (F) groups, performed on means of 3 stimuli x 2 trials blocks. p<0.05*
242 *in green, p<0.1 in yellow, p≥0.1 in white.* ***J)*** *The same as I) comparing Control (E) and 1 mM D-βHb+AIR*
243 *(H) groups. No significant differences, p=0.067 to p=0.99.* ***K)*** *The same as I) comparing AIR (F) and 0.1*
244 *mM D-βHb+AIR (G) groups. No significant differences, p=0.41 to p=0.99.* ***L)*** *The same as I) comparing AIR*
245 *(F) and 1 mM D-βHb+AIR (H) groups.*

246 Changes in the CV of the observed magnitude and resulting differences in input timing would
247 likely desynchronize the hippocampal circuit. Therefore, we investigated whether latency of FVs
248 changes during stimulation with 20 pulse trains.

249 In all treatment groups, the early FVs showed ~-0.2 ms improvement in latency. During the first 3
250 min, all experimental groups were comparable and exhibited the same pattern of latency changes.
251 Afterwards, AIR and 0.1 mM D-βHb+AIR groups displayed progressively more prominent delays
252 than Control, while Controls and 1 mM D-βHb+AIR groups remained comparable. During AIR, we
253 observed the largest delays [**Fig. 3E-F, Fig. 3I, L**; at 15 min, stim. 9-11: +2.69 ± 0.84 ms, Control
254 vs. AIR, p=0.0077; 2.64 ± 0.94 ms, AIR vs.1 mM D-βHb+AIR, p=0.020]. The escalating nature of
255 the delays during the stimulation suggests that the detrimental effects of AIR are further
256 exacerbated over longer periods of time.

257

258 *3.4 AIR increases membrane resistance (R_m) without affecting other intrinsic membrane*
259 *properties of CA1 pyramidal neurons. D-βHb treatment under AIR does not rescue R_m to normal*
260 *levels.*

261 Results presented above [**Fig. 2**] indicate that AIR might negatively impact the membrane
262 properties of hippocampal neurons, therefore we sought to identify the properties most vulnerable
263 to AIR and test DβHb as a recovery agent. Based on dose-response results from the field potential
264 studies, we selected 1 mM D-βHb for use in patch clamp experiments, testing the effects of AIR
265 and D-βHb on intrinsic membrane properties of the CA1 pyramidal neurons (membrane
266 resistance, R_m; membrane capacitance, C_m, and resting membrane potential, V_{rest}), and their spike
267 thresholds. We found significantly increased R_m of the CA1 pyramidal neurons in the AIR group
268 compared with Controls [**Fig. 4B**, +43.24 ± 3.73%, p=1.41E-07], which remained increased in the
269 presence of 1 mM D-βHb [**Fig. 4B**, +27.86 ± 8.93%, p=0.030], while AIR and 1 mM D-βHb+AIR
270 groups were similar (p=0.31). Interestingly, neither C_m [**Fig. 4C**, 114.25 ± 9.73, 115.52 ± 9.26,

132.20 ± 9.46, Control, AIR, D-βHb+AIR, respectively, p=0.32], spike threshold [**Fig. 4E**, -46.31 ± 0.76, -44.53 ± 0.80, 44.64 ± 0.73, p=0.17] nor $V_{rest.}$ [**Fig. 4F**, -67.26 ± 1.17, -63.57 ± 1.38, -65.11 ± 0.99, p=0.093] were significantly affected by either AIR or D-βHb+AIR treatments.

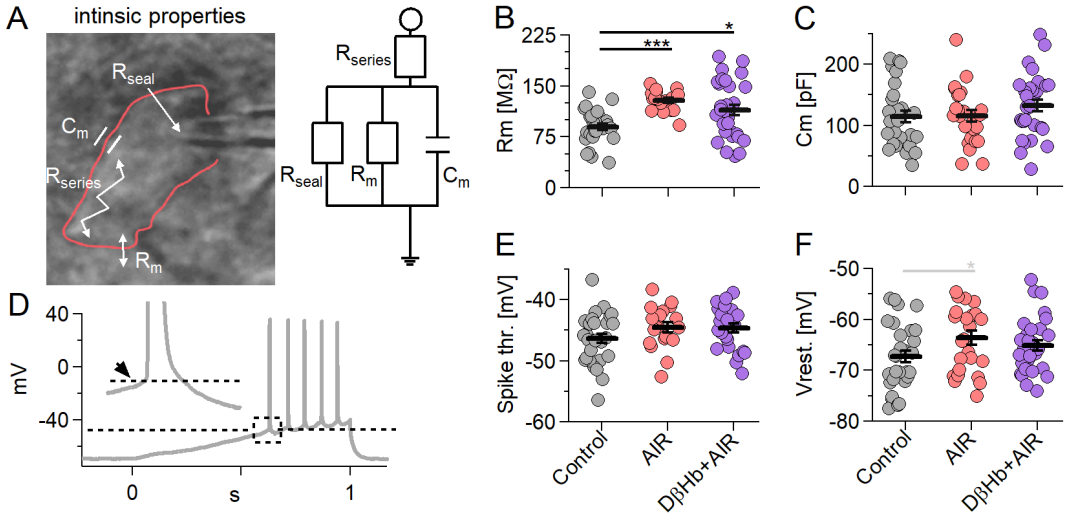

Figure 4: ***Membrane resistance (R_m) increases during AIR and is not reversed by D-βHb. Other intrinsic properties did not change under either condition.***

A) On the left: A CA1 pyramidal neuron recorded in whole-cell patch clamp mode (outlined in red) with resistances and capacitance within the cell. On the right: A simple electric circuit diagram of the cell with the same resistances. **B)** Scatter plots of CA1 pyramidal neuron R_m, compared between the experimental groups. Each colored circle represents a value recorded in a single cell. Control in gray, AIR in light red, 1 mM D-βHb+AIR in purple. Vertical black bars represent mean ± SEM. **C)** Scatter plots of CA1 pyramidal neurons C_m, compared between the experimental groups. The plots and coloring are identical to B). No significant differences (p=0.32). **D)** Representative example of a 300pA ramp current injection performed in a Control CA1 pyramidal neuron. The dashed line marks the onset (spike threshold) of the first AP. The inset shows the magnified AP with the arrow pointing to the onset. **E)** Scatter plots of CA1 pyramidal neuron spike thresholds, compared between the experimental groups. The plots are identical to B). No significant differences (p=0.17). **F)** Scatter plots of CA1 pyramidal neurons RMP (V_{rest}), compared between the experimental groups. The plots and coloring are identical to B). No significant differences (p=0.09). Control n=28, N=22; AIR n=25, N=17; 1 mM D-βHb+AIR; n=30, N=16. In black, *p<0.05; **p<0.01; ***p<0.001; in gray *p<0.1.3.3 AIR adversely affects input timing, restored by high D-βHb concentrations.

3.5 AIR increases the frequency of spontaneous vesicular release at CA1 synapses (sEPSCs) and mildly increases sEPSC amplitudes. D-βHb does not reverse the increase in frequency but

295 *mildly decreases sEPSC amplitudes.*

296 Recovering the membrane back to resting potential during synaptic transmission is the most
297 energy-consuming neuronal process (~% of total ATP produced [40]), therefore, we tested for
298 changes in the frequency and magnitude of quantal EPSCs that might explain the ~35% decrease
299 in fEPSP amplitudes reported above (**Fig.1-3**).

300 AIR significantly increased the frequency of sEPSCs, nearly doubling the number of events
301 compared with the Control [**Fig. 5A,B**; 0.53 vs. 0.96 Hz, +0.42 ± 0.12 Hz, p=0.0031]. Interestingly,
302 D-βHb failed to rectify the increased qEPSC frequency [**Fig. 5A,B**; D-βHb+AIR 0.93 vs. AIR 0.96
303 Hz, 0.021 ± 0.15 Hz, p=0.99; D-βHb+AIR vs. Control, +0.40 ± 0.12 Hz, p=0.0091]. However, the
304 amplitude, rise-time, and sEPSCs decay time showed no significant differences between the
305 groups [**Fig. 5C-E**].

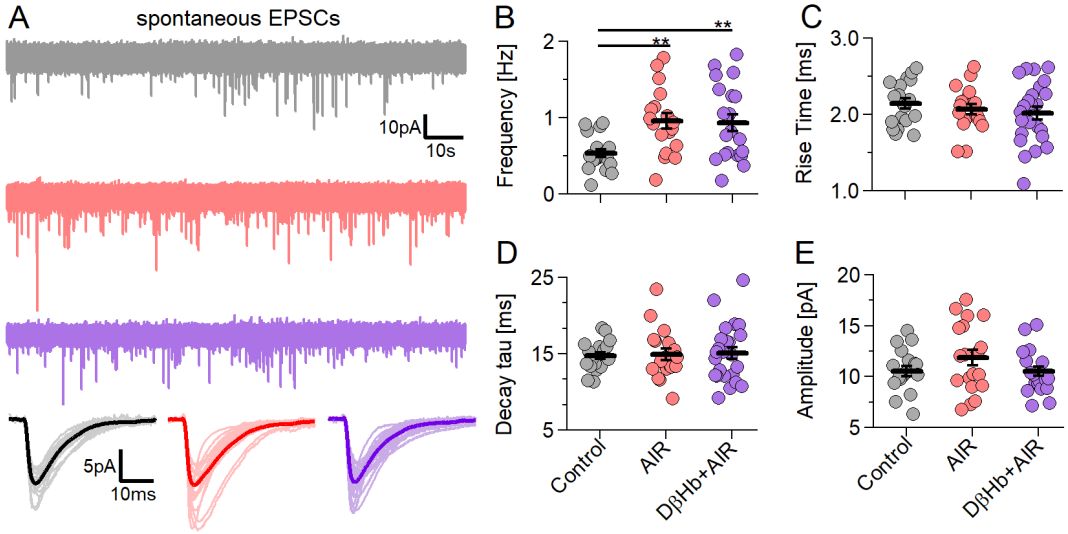

306 **Figure 5: *AIR increased sEPSC frequency without altering sEPSC properties and D-βHb (1*
307 ***mM) does not reverse this effect.***

308 ***A)*** *Representative examples of the first 2 min of sEPSC recorded in CA1 pyramidal neurons, voltage*
309 *clamped at V_h= -70 mV (Control in gray; AIR in red; 1.0 mM D-βHb+AIR in purple). Below: averaged sEPSC*
310 *waveforms from individual cells (light color) and the group mean (full color).* ***B)*** *Scatter plots of the sEPSCs*
311 *frequency recorded in CA1 pyramidal neurons, compared between the experimental groups. Each colored*
312 *circle represents frequency recorded in a single cell. Labels as in A) Vertical black bars represent mean ±*
313 *SEM. *p<0.05.* ***C)*** *Scatter plots of the sEPSC 20-80% rise times, as in B). No significant differences*
314 *(p=0.51).* ***D)*** *Scatter plots of the sEPSC decay tau times, as in B). No significant differences (p=0.98).* ***E)***
315 *Scatter plots of the sEPSC amplitudes, as in B). No significant differences (p=0.21). Control n=19, N=19;*
316 *AIR n=19, N=14; 1 mM D-βHb+AIR, n=23, N=16. **p<0.01.*

317 Given the change in R_m, the lack of significant changes in the amplitudes is surprising. Several
318 studies utilizing different metabolic challenges, such as food deprivation [41] and inhibition of

319 glycolysis [42], showed an increase in mEPSC/sEPSC amplitudes, therefore, we decided to
320 investigate our sEPSCs in more detail. In most central synapses, the distribution of
321 mEPSC/sEPSC amplitudes shows several peaks related to simultaneous release of multiple
322 quanta of neurotransmitter [43], with each subsequent peak linked to an increasing number of
323 concurrent sEPSCs. Capitalizing on the multiplicative nature of this process, we assumed that
324 small changes in amplitudes [**Fig. 5E**] would scale up. We detected 2-4 distinct peaks in ~85% of
325 the analyzed cells [**Fig. S3A-C**], with no differences between the groups in the number of cells
326 with multi-peak distributions [**Fig. S3C**; 89.5% in Control; 84.2% in AIR, 87.5% in D-βHb+AIR]. In
327 line with our initial assumptions, the scaled amplitudes revealed differences between the groups
328 [**Fig. S3E**]: AIR group had significantly higher amplitudes than D-βHb+AIR [p1: p=0.048; p2:
329 p=0.0054; p3: p=0.0038; p4: p=0.021] and also tested as different from Controls at peak 3
330 [p=0.007]. Control and D-βHb+AIR groups did not show significant differences at any point [**Fig.
331 S3E]**, despite the same sEPSC frequency as AIR.

332 We further validated those findings by comparing the normalized amplitude distributions [**Fig.
333 S3F-I**]. Within the range correlating to peak 2 – peak 4 (sEPSC of ~20pA or more), the AIR group
334 had a significantly higher number of large events (15.19% of total) when compared to Control
335 (7.65%) and D-βHb+AIR (9.48%) [**Fig. S3F-I**], while Control and D-βHb+AIR groups showed little
336 consistent difference. This result suggests that during AIR, the elevated frequency of events
337 increased the probability of multi-vesicular events occurring, further exacerbated by the ~20%
338 increase in R_m. On the other hand, D-βHb+AIR produced a distribution resembling Control, as if
339 the vesicles had lower glutamate content, as suggested by literature [44,45].

340

341 3.6 *AIR slightly changes the firing pattern of hippocampal pyramidal neurons and causes*
342 *increased membrane depolarization with input. Those effects are reversed by D-βHb, which also*
343 *increases AP amplitudes.*

344 The action potential generation and subsequent recovery of V_m to resting levels entail a large part
345 of the energy budget of pyramidal neurons (~41% of all produced ATP [40]), therefore, we
346 investigated whether pyramidal neurons retain their input-output curves (I-O curve) under AIR
347 and how D-βHb alleviates AIR effects.

348 First, we focused on the firing frequency [**Fig. 6A**]. Cells under AIR showed increased firing at
349 lower current injections than D-βHb+AIR [**Fig. 6B**, 75–150 pA, p=0.0038 to 0.050], but with the
350 same maximal firing rate. These results suggest that the cells activate earlier under AIR than in
351 the Control or D-βHb+AIR conditions. To test this further, we measured the maximum
352 depolarization attained by each neuron during the final 5 ms of each current injection step [**Fig.
353 6D**]. AIR neurons had slightly higher depolarization with each injection step compared to Controls
354 [**Fig. 6E,F**; p=0.0027 to 0.048] or D-βHb+AIR [**Fig. 6E,F**; p=0.0029 to 0.042].

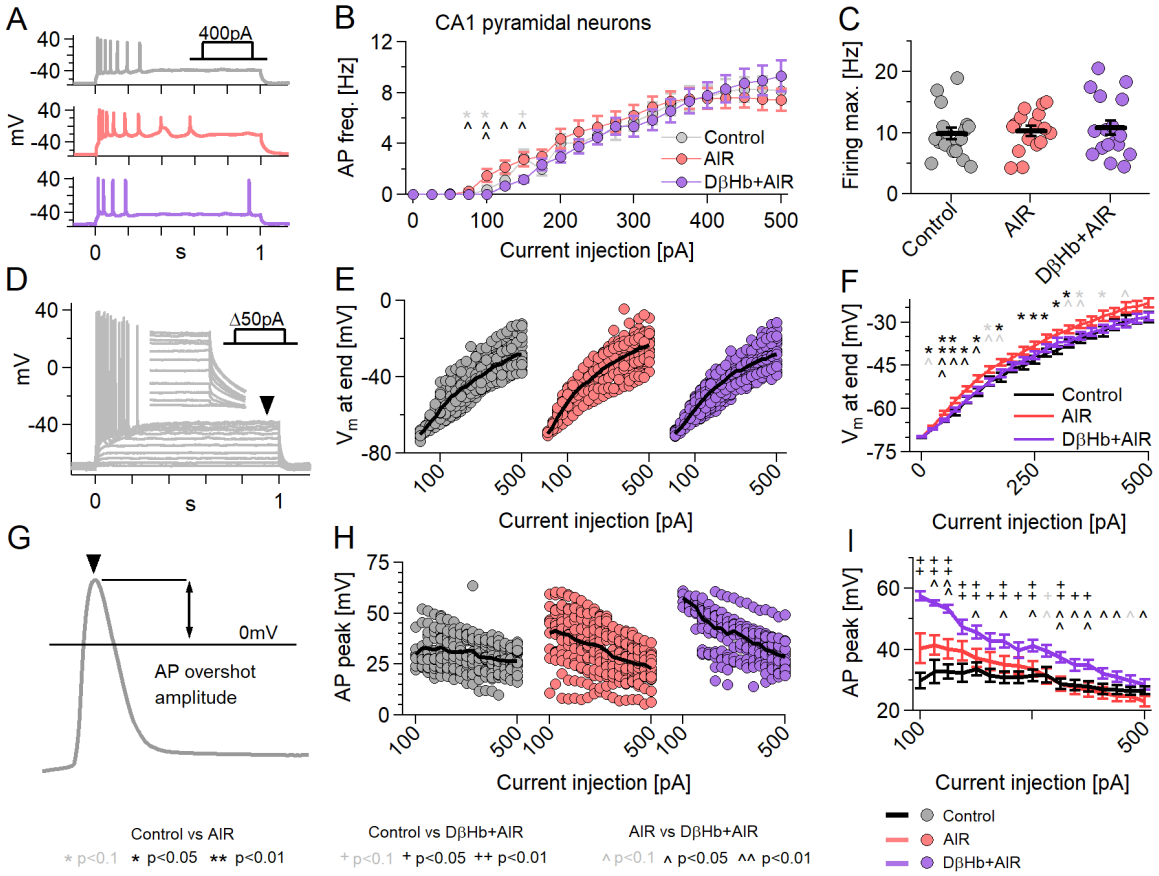

Figure 6: *Neuronal firing is mildly affected by AIR and reversed by DβHb, with DβHb increasing AP overshoot amplitudes.*

A) *Representative examples of responses to 400 pA square current injections into Control (gray), AIR (red), and 1 mM D-βHb+AIR (purple) CA1 pyramidal neurons, held at V_h=-70 mV.* ***B)*** *I-O curves of CA1 pyramidal neurons receiving 21, Δ+25pA injections (max. 0 pA; V_h=-70 mV). Circles represent group mean ± SEM. * Control vs. AIR, + Control vs. 1 mM D-βHb+AIR, ^ AIR vs. 1 mM D-βHb+AIR. *,+,^ in black p<0.05; **,++,^^ in black p<0.01; *,+,^ in gray p<0.1; ANOVA****C)*** *Maximum firing rate of the pyramidal neurons in B). Circles represent single neurons; black bars represent group means ± SEM. No significant differences (p=0.778, ANOVA).* ***D)*** *Example of responses to Δ+pA square current injections into a control pyramidal neuron. The arrowhead and inset mark the final membrane depolarization (V_m, last 5 ms of the step).* ***E)*** *V_m at the current injections from B).* ***F)*** *Group means ± SEM of V_m from E). Statistical tests and labels are identical to B). Control n=23, N=20; AIR n=20, N=14; 1 mM D-βHb+AIR n=22, N=16.* ***G)*** *Example of AP overshoot measurement. Black line marks V_m= 0 mV.* ***H)*** *Averaged AP overshoot amplitudes from B).* ***I)*** *Group means ± SEM of overshoot amplitudes from H). Statistical tests and labels are identical to B). In all comparisons Control n=23, N=20; AIR n=20, N=14; 1 mM D-βHb+AIR, n=22, N=16.*

Next, we investigated the averages of AP peak amplitudes [**Fig. 6G**], per step [**Fig. 6H**]. Surprisingly, D-βHb+AIR neurons showed the largest amplitudes, consistently elevated

throughout the injections, when compared to Controls or AIR, while AIR neurons remained comparable to Controls [**Fig. 6I**, p=0.0017 to 0.036, AIR vs. Control; p=0.0093 to 0.044, AIR vs. 1 mM D-βHb+AIR].

3.7 *AIR increases AP decay time, while D-βHb accelerates the AP rise without reversing the AIR-induced slower AP decay.*

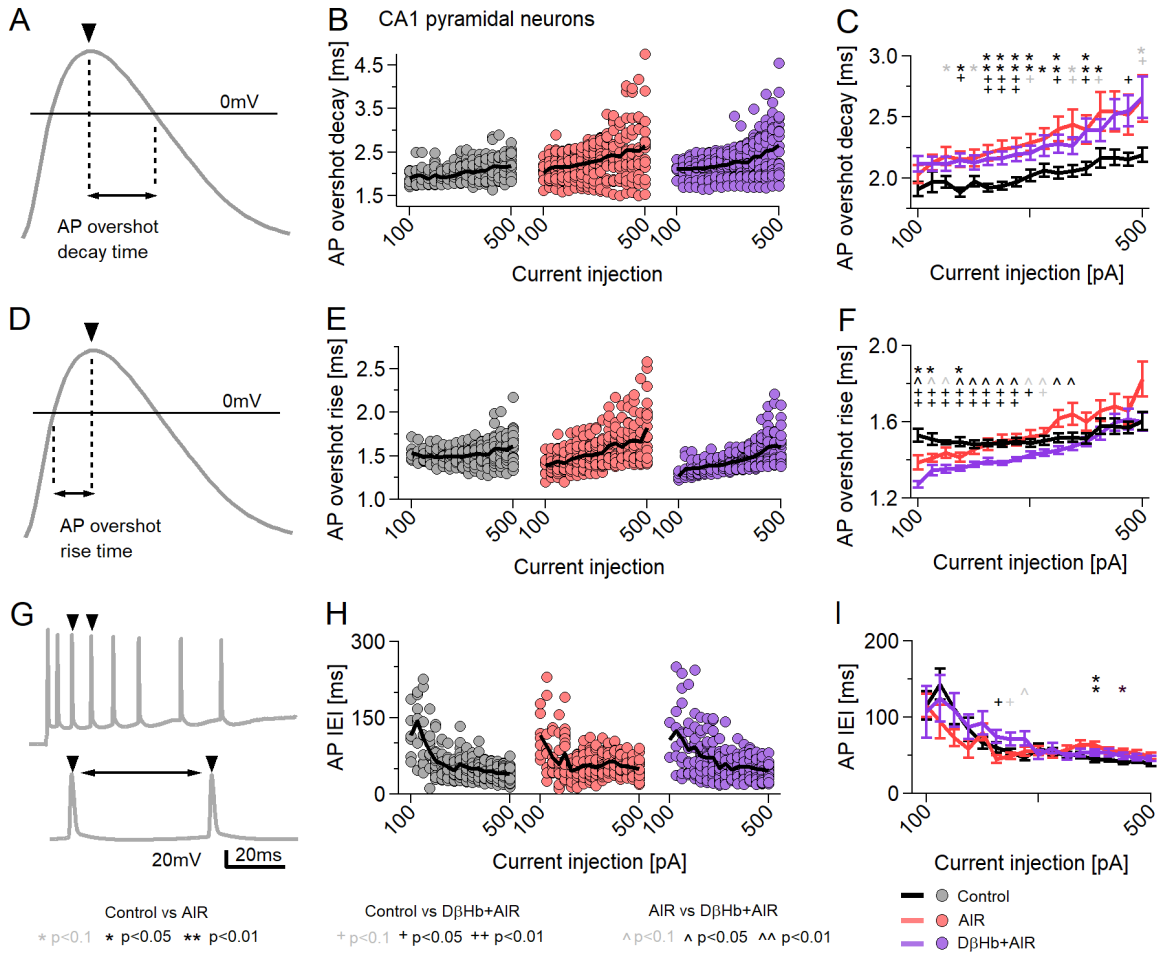

Figure 7: *AP decay times change during AIR and DβHb + AIR but DβHb + AIR APs have faster rise times.*

A) *Example of AP decay time measurement. Black line marks V_m= 0mV.* ***B)*** *Mean AP decay times for the current injections. Circles represent averaged amplitudes in single neurons. Black lines represent group means.* ***C)*** *Group means ± SEM of AP decay times from B). Statistical tests and labels are identical to B).* ***D)*** *Example of AP decay time measurement. Black line marks V_m= 0mV.* ***E)*** *Averaged AP rise times for the current injections in B). Circles represent averaged amplitudes in single neurons. Black lines represent group means.* ***F)*** *Group means ± SEM of AP rise times from B). Statistical tests and labels are identical to*

*B). **G)** An example of the AP IEI measurement. The double arrow marks the latency between AP peaks. **H)** Averaged IEI recorded during the injections in B). Each point represents the average of IEIs recorded at each step in a single neuron. The black line represents the group mean. **I)** Group means ± SEM of averaged IEI. *,+,^ p<0.05; ANOVA. In all comparisons Control n=23, N=20; AIR n=20, N=14; 1 mM D-βHb+AIR, n=22, N=16.*

We next proceeded to investigate other properties of the APs: decay time (from the overshoot peak to 0 mV) [**Fig. 7A-C**] and rise time (from 0 mV to the overshoot peak) [**Fig. 7D-F**]. We found that Control neurons had significantly lower average AP decay times when compared to AIR [**Fig. 7B,C**; p=0.047 to 0.0019] and D-βHb+AIR conditions [**Fig. 7B,C**; p=0.041 to 0.0023], across almost all current injection steps. AIR and D-βHb+AIR cells did not significantly differ at any point [**Fig. 7B,C**; p=0.32 to 0.99]. D-βHb+AIR cells demonstrated faster rise times compared to Control [**Fig. 7E,F**; p=0.000094 to 0.0025] and AIR cells [**Fig. 6E,F**; p=0.047 to 0.0052] in the majority of the injection steps. Interestingly, AIR cells exhibited slightly faster AP rise times exclusively at the lowest current injections [**Fig. 4 N,O**; p=0.012 to 0.035]. These slightly faster APs were likely due to earlier activation of the cells, as shown in [**Fig. 6B-C, E-F**]. **Fig. 7Fig. 6**

Finally, as we did not observe significant differences in firing frequency among the groups [**Fig. 6B,C**], we examined variations in the timing of AP firing based on the intervals between consecutive APs (AP Inter Event Interval, AP IEI) [**Fig. 7G**], but we found no clear changes in the AP IEI [**Fig. 7H,I].**

3.8 *AP adaptation is impaired during AIR, with AP amplitudes showing steeper declines, and is not reversed by D-βHb.*

The amplitudes of the AP overshoot, decays, and rise times demonstrated steeper slopes in the AIR and D-βHb+AIR groups. The properties of APs during neuronal firing undergo dynamic changes, commonly referred to as spike adaptation or spike frequency adaptation [46] and in our experiments, we see evidence that GLUT4 antagonism intensified these changes.

To test this observation, we compared peak amplitudes of the first APs [**Fig. S4A-D**], the averaged APs [**Fig. 6G-I**, **Fig. S4E**] and the final APs during current injections [**Fig. S4F**]. The first APs represents neuronal firing after rest (10s between subsequent injections), while the average and final AP – after energy expenditure. As expected, the first APs displayed minimal changes in amplitude during injections [**Fig. S4D**], with D-βHb+AIR exhibiting consistently larger amplitudes than the Control. AIR, also showing elevated amplitudes, did not differ significantly from either the Control or D-βHb+AIR groups. For the final APs, we observed a sharp decline in amplitude scaling with injected current [**Fig. S4F**] in both AIR and D-βHb+AIR groups. Control showed lower amplitudes than D-βHb+AIR at 100-300pA injections (p=0.040 to p=6E-05) and remained comparable to AIR up until the very last, large, 400-0pA injections (p=0.032 to p=0.0011), when AIR APs significantly declined [**Fig. S4F**]. AIR and D-βHb+AIR remained consistently different.

423 Linear fits to the average AP amplitudes revealed significantly steeper declines [**Fig. S4G,H**;
424 p=0.00039, AIR vs Control; p=0.0012, D-βHb+AIR vs Control], indicating that prolonged neuronal
425 activity is heavily affected by AIR.

426

427 3.9 *Changes in AP decay and rise times translate into differences in the widths of FVs.*

428 In our initial analysis of the field potential (FV) data, our focus was solely on the amplitudes of the
429 biological signals. Consistently, we found no significant changes in the FV amplitudes [**Fig. 1F,**
430 **2C, 3E-G**], which supports our findings on AP overshoot amplitudes [**Fig. 6G-I**] (with the exception
431 of D-βHb+AIR group). Based on these results, we further investigated whether the changes in AP
432 decay and/or rise times also corresponded to changes in FV widths during train stimulation [**Fig.**
433 **S5**].

434 Consistent with our findings on AP decay/rise times [**Fig. 7A-F**], AIR consistently exhibited the
435 widest FVs throughout the stimulation followed by the Control group, with 1mM D-βHb+AIR FVs
436 as the narrowest [**Fig. S5D**]. We found differences between AIR and Control (p=3.94E-06 to
437 0.049), and AIR and 1mM D-βHb+AIR (p=4.04E-05 to 0.046) throughout the whole stimulation
438 period, while Control and 1mM D-βHb+AIR were not different (p=0.079 to 0.99), supporting our
439 AP decay/rise time findings [**Fig. 6G-I**].

440

441 3.10 *With abolished GABAergic inhibition, AIR strongly decreased firing rates of CA1 pyramidal*
442 *neurons and fast-spiking interneurons (FSI), which were not rescued by DβHb.*

443 As the next step, we investigated the properties of CA1 pyramidal neurons and FSIs after
444 pharmacologically abolishing AMPA/kainate excitatory (NBQX) and fast GABAergic inhibitory
445 (gabazine) transmission [**Fig. S6**].

446 We first recorded the firing frequency of CA1 pyramidal neurons [**Fig. S6A,B**] at different
447 activation levels [**Fig. S6C,D**], finding that AIR prominently decreased their firing rate, when
448 compared with Control [**Fig. S6C**, p=0.024 to 0.0053]. Surprisingly, the application of 1 mM D-
449 βHb during AIR resulted in a stronger reduction in firing rate, when compared with Control [**Fig.**
450 **S6E**, p=0.000027 to 0.035]. AIR and D-βHb+AIR results remained similar throughout the
451 injections [**Fig. S6E**]. However, all groups differed significantly with respect to the maximum firing
452 rate, with Control having the highest (31.03 ± 3.43) and D-βHb+AIR having the lowest (13.17 ±
453 2.05) firing rates.

454 Next, we examined CA1 FSIs using the same drug conditions [**Fig. S6E,F**]: AIR decreased the
455 firing rate of FSIs compared with Control [**Fig. S6G**, p=0.012 to 0.048], not reversed by D-βHb
456 [**Fig. 5S6H**, p=0.00017 to 0.035]. As for pyramidal neurons, the FSIs for AIR and D-βHb+AIR

457 groups remained mostly comparable [**Fig. S6G**]. None of the groups differed in the maximum
458 firing rate [**Fig. S6H**, p=0.068].

459

460 3.11 *Hodgkin-Huxley model predicts that impairments in Na^+/K^+ ATPase activity result in more*
461 *depolarized V_{rest}, lower AP overshoot (V_a), and increased neuronal firing.*

462 Here we aim to explain the previous observations of dysregulated firing dynamics in response to
463 AIR. We hypothesize that Indinavir restricts the energy supply of neurons and thus impairs the
464 neuronal Na^+/K^+ ATPase. To test this hypothesis, we developed a computational model of an
465 isolated CA1 neuron in the absence of inhibition and toggled Na^+/K^+ ATPase activity through the
466 enzyme kinetic parameter v_{ATPase}^{max} (see supplementary methods, **Fig. S7**). **Figs. S7A,B** (at two
467 different temporal scales) shows the predicted changes in neuronal firing dynamics when the
468 Na^+/K^+ ATPase is impaired. Such an impairment predicts the depolarization of the resting
469 membrane potential (**Fig. S7C**) and is consistent with trends of our I/O curves (**Fig. 4F**).
470 Furthermore, this modeled depolarization reduces the magnitude of membrane potential shift
471 required for an action potential. Consequently, the model predicts increased firing frequency (**Fig.**
472 **S7D**). Finally, the model predicts that the Na^+/K^+ ATPase should act more slowly to recover ion
473 gradients after an AP, causing the amplitude of subsequent APs to decline progressively with time
474 (**Figs. S7E,F**). Such an amplitude decrease is consistent with the trends in measured conduction
475 velocity (**Fig. 2**).

476

477 4. **Discussion**

478 Central insulin resistance impairs cognitive performance and promotes hippocampal
479 neurodegeneration and memory loss [47,48]. Our present results highlight the adverse effects of
480 GLUT4 inhibition on synaptic function and LTP, in accord with findings that acute and chronic
481 blockade of GLUT4 are detrimental to performance on hippocampal-mediated memory tasks, thus
482 suggesting that GLUT4 is critical for acquisition and consolidation of memory [8,13]. Memory
483 formation is promoting GLUT4 incorporation into the membrane, resulting in increased glucose
484 flux into neurons [13,49]. This process enables increased metabolic support during high demand.
485 Crucially, most GLUT4s localize in the perikaryon [50,51], likely in close proximity to axo-somatic
486 synapses, which are associated with synaptic plasticity and long-term memory (LTM). Indeed,
487 prolonged blockade of the GLUT4 glucose transporter in the brain results in impaired formation
488 of LTM [13] and decreased levels of hippocampal BDNF [52]. Moreover, hypoglycemia negatively
489 affects memory performance and cognition [53,54, however, see 13]

490 In this study, we found that AIR increased the frequency of sEPSC events, in line with the
491 previously published data showing similar increases during food deprivation [42], inhibition of
492 glycolysis [41] and ischemia [55], likely due to hypoglycemia-driven Ca^{2+} accumulation at the
493 presynapse [41,55]. The same studies suggest that presynaptic glycolysis is essential for

494 maintaining synaptic transmission, even at a low frequency, and that mitochondrial respiration
495 cannot substitute it. Normally, glycolysis meets approximately one-third of the energy budget at
496 presynaptic terminals, thus sustaining low-frequency transmission. In addition, impaired
497 glycolysis leads to slower, broader, and smaller AP waveforms, and a depolarization of the resting
498 membrane potential [42]; results which are consistent with ours. Interestingly, D-βHb+AIR
499 treatment, which showed the same increase in the frequency of sEPSCs as AIR, had the lowest
500 sEPSC amplitudes [**Fig. S3E**]. This result suggests a reduction in the quantal content of synaptic
501 vesicles and is consistent with reports of lowered conversion of glutamate to aspartate under
502 ketosis [44,45].

503 Although the results of our computational models are consistent with the observed changes in
504 resting state membrane potential and firing frequency during AIR, there were seemingly
505 contradicting results with respect to AP peak amplitude. Specifically, we measured no significant
506 changes to average AP overshoot amplitudes during AIR, our model predicted a decrease due to
507 energy constraints. In the model we did not consider a progressive decline in available energy,
508 which is suggested by the steeper AP adaptation [**Fig. S4**]. Moreover, neurons may compensate
509 for the energetic limitations by increasing R_m (as reported in 42), while our model assumes that
510 R_m remains unchanged. When those factors are accounted for, the model and experimental data
511 agree: during periods of extensive activity, energy reserves in neurons are progressively depleting
512 and, provided that the neuron fired multiple APs in short succession, the negative effects of
513 hypoglycemia overcome compensatory R_m increases and AP amplitudes decline below Control
514 levels [**Fig. S4**]. Furthermore, we used the maximal Na^+/K^+ ATPase activity as a surrogate for
515 ATP availability, and we relied on literature estimates of kinetic and thermodynamic rate
516 constants. A more direct approach might consider ATP concentration as an input variable, were
517 such experimental data available.

518 Our model aiming to establish the underlying causes of the changes in conduction velocity
519 investigated resting membrane potential (V_{rest}) and AP peak amplitude as two critical factors. The
520 model explains CV recovery and increases during D-βHb+AIR treatment, since the measured AP
521 peak amplitudes remain consistently elevated and V_{rest} changes are negligible, but fails for AIR
522 alone, where AP amplitudes remain comparable to Control and V_{rest} tends to depolarize. This
523 discrepancy might reflect the simplistic nature of our model, which neglects complex ion
524 dynamics, altered membrane permeability or synaptic processes.

525 The ketogenic diet has served for decades to treat epilepsy and has an emerging wide range of
526 therapeutic applications [30]. Possible mechanisms include modulation of ATP-sensitive K^+
527 channels (K_{ATP}), free fatty acid receptor 3 (FFAR3/ GPR41) activation, promotion of GABA
528 synthesis, and epigenetic modifications [56]. The action of D-βHb in modulating potassium flux
529 through K_{ATP} channels may be most relevant in the present context [57], since K_{ATP} activation
530 results in decreased neuronal firing rates [58,59] and prevented picrotoxin-induced epileptiform
531 activity in the hippocampus [60] and may explain present findings that firing rates and membrane
532 depolarization remained at control levels in the presence of 1 mM D-βHb during AIR (despite
533 elevated R_m).

534 D-βHb is a precursor of glutamine, which promotes increased GABA levels, as seen in studies of
535 the ketogenic diet in clinical epilepsy [61]. D-βHb also directs glutamate towards GABA production
536 by reducing the conversion of glutamate to aspartate [44,45]. In addition, D-βHb has a direct effect
537 on the vesicular glutamate transporter VGLUT2, by inhibiting Cl^- dependent glutamate uptake.
538 VGLUT2 is critical for glutamate excitatory transmission in CA3-CA1 and its conditional VGLUT2
539 knock-out results in impaired spatial learning and reduced LTP [62]. Together with the increased
540 formation of GABA and/or GABA derivatives, VGLUT2 inhibition could further reduce glutamate
541 excitatory transmission [63].

542 The present results have important implications for the treatment of conditions such as type 2
543 diabetes, metabolic syndrome, and seizure disorders that involve insulin hyposensitivity.
544 According to NIH estimates, ~30% of Americans today display symptoms of prediabetes, a
545 percentage expected to increase in the nearby future. Together with the longer average lifespans
546 and demographic changes leading to an expansion in the aging population, obtaining insights into
547 the outcomes of metabolic dysfunction and its potential treatment becomes a more pressing
548 matter each day. Our results provide a unique insight into the potential use of KBs as an
549 inexpensive and relatively risk-free treatment for metabolic disorders and insulin resistance.
550 Medical researchers can use this information to discover new targets for treatment and develop
551 therapies that are more effective. Further research in this area could inform novel treatment
552 approaches that address the complex effects of metabolic disorders on brain health.

553

554 5. **Materials and Methods**

555 5. 0 *Mice*

556 Breeding pairs of transgenic GAD2Cre/GCamp5gTdTomato, Thy1/GCamp6fTdTomato, and
557 C57BL/6J mice were originally obtained from The Jackson Laboratory (stocks 010802, 024477,
558 024339) or Charles River Laboratories and bred in-house under standard conditions of 12-12
559 hours light-dark cycle, with food and water available *ad libitum*. The Institutional Animal Care and
560 Use Committee approved all experiments. Mice of both sexes aged between 30 and 60 days
561 (P30-P60) were used in all experiments.

562

563 5.1 *Electrophysiology – slice preparation.*

564 Coronal brain slices containing the hippocampus were used in all recordings. Mice were deeply
565 anesthetized with a mixture of isoflurane and air (3% v/v), decapitated, and their brains extracted
566 and cut using a Leica VT1200S vibratome into 300 µm-thick slices in ice-cold ACSF solution
567 containing (in mM): 230 sucrose, 1 KCl, 0.5 $CaCl_2$, 10 $MgSO_4$, $NaHCO_3$, 1.25 NaH_2PO_4, 0.04 Na-
568 ascorbate, and 10 glucose; 310 ± 5 mOsm, pH adjusted to 7.35 ± 5 with HCl, and, gassed with

569 carbogen (95% O_2, 5% CO_2) for at least 30 min before use. The slices were then transferred to a
570 Zbicz-type BSC-PC submerged slice chamber (Harvard Apparatus, USA) filled with artificial
571 cerebrospinal fluid (ACSF) containing (in mM): 124 NaCl, 2.5 KCl, 2 $CaCl_2$, 2 $MgSO_4$, 26 $NaHCO_3$,
572 1.25 NaH_2PO_4, 0.04 Na-ascorbate, and 10 glucose; 305 ± 5 mOsm/kg, pH adjusted to 7.35 ± 0.05
573 mOsm/kg, gassed with carbogen and prewarmed to 32 ^oC. The slices were allowed to recover in
574 the warm ACSF for 15 min, whereupon the heating was switched off, and the chamber gradually
575 cooled down to room temperature (RT; 23 ± 2 ^oC) over 45 min.

576 Following the recovery, individual slices were transferred to another BSC-PC chamber filled with
577 gassed ACSF and a mixture of drugs (Indinavir 0.1 mM; Indinavir 0.1 mM and either 0.1- or 1-mM
578 DβHb), where they were incubated for 60 ± 15 min. Next, the slices were transferred to a
579 submerged recording chamber mounted on an upright microscope stage (E600FN, Nikon, Japan)
580 equipped with infrared differential interference contrast (IR-DIC) filters. The slices were kept at
581 RT and superfused continuously with gassed ACSF delivered by a peristaltic pump at a steady
582 rate of ~2 ml/min.

583

584 *5.2 Field potential recordings.*

585 Evoked field potential responses were triggered with an isolated pulse stimulator (Model 2100,
586 AM Systems, USA) using a CBARC75 concentric bipolar electrode (FHC, USA) placed between
587 CA3 and CA1. The recording electrode was placed 300 ± µm away for the recordings of CA1 FV
588 and fEPSP. During the recordings of axonal conduction velocity (CV), the electrodes were 300 to
589 900 ± 50 µm apart, and up to 6 different sites were recorded. All stimulation paradigms were
590 applied every 20 s as biphasic rectangular pulses of 240 µs total duration, 50 ± 5 V strength (~60
591 ± 10% of the maximum response size), and a between-stimuli frequency of 25 Hz (40 ms).

592 During non-CV recordings, three different types of stimulation were applied: paired, 20 stimuli,
593 and stimuli trains, repeated every 20 s for a total period of 20 min in each case. After each train
594 stimulation, the slice was allowed to recover for 20 min under paired stimulation.

595 Recording pipettes were pulled from borosilicate glass capillaries (ID 0.86, OD 1.5, BF1-86-10,
596 Sutter Instruments, USA) on a vertical PC-100 puller (Narishige, Japan) and filled with 6% NaCl
597 (in H_2O, 1.02 M). Only pipettes with a resistance of 0.2-1.0 MΩ were used. Recording pipettes
598 were allowed to rest at the recording site for 10 min to equilibrate before the start of a recording.
599 All recorded signals were acquired using a MultiClamp 700B amplifier (Molecular Devices, USA),
600 Bessel-filtered at 2 kHz, and digitized at a sampling frequency of 10 kHz using an Axon Digidata
601 1440A digitizer (Molecular Devices, USA).

602

603 *5.3 Whole-cell patch-clamp recordings.*

604 Pyramidal neurons of the hippocampal CA1 region were selected for recordings based on their
605 general morphology and position within the pyramidal layer. As an additional verification, recorded
606 cells were screened for $GAD2^+$-driven tdTomato fluorescence. Cells that displayed any level of
607 tdTomato fluorescence were rejected.

608 Patch pipettes were pulled from borosilicate glass capillaries (BF1-86-10, Sutter Instruments,
609 USA) on a vertical puller (PC100, Narishige, Japan). Pipettes had a resistance of 6–8 MΩ when
610 filled with an internal solution containing (in mM): 136 K-gluconate, 4 Na_2ATP, 2 $MgCl_2$, 0.2 EGTA,
611 10 HEPES, 4 KCl, 7 di-triphospho-creatine, 0.3 Na_3GTP; 280–290 ± 5 mOsm/kg, titrated to pH
612 7.3 ± 0.05 with KOH.

613 During recordings in voltage clamp (VC), cells were clamped at the holding potential (V_h) = −70
614 mV with a Multiclamp 700B amplifier (Molecular Devices, USA). Liquid junction potential was not
615 corrected. All cells were compensated for pipette capacitance. During VC experiments, series
616 resistance (R_s) was not compensated. During recordings in current clamp (CC), a holding current
617 was applied to the cells to maintain membrane potential at V_h = -70 ± 3 mV. All cells were bridge-
618 balanced at % of R_s. Cell capacitance was not compensated in either mode. Immediately after
619 establishing the whole-cell configuration, the cell was kept in I=0 mode to monitor the resting
620 membrane potential (V_{rest}) over a period of ~120 to 180 s. The average value of V_{rest} over this
621 period is reported as the neuron's V_{rest}.

622 During the recordings, every 5 to 10 min a series of 10 square voltage steps of −10 mV was
623 apllied to monitor changes in the R_s (Vh = -70 mV). All whole-cell currents in response to voltage
624 steps were low-pass filtered at 10 kHz with a Bessel filter and sampled at 20 kHz frequency (Axon
625 Digidata 15B, Molecular Devices, USA). For inclusion in the final dataset, recordings had to meet
626 3 criteria: 1) R_s after any recorded protocol could not increase by more than 20% compared to the
627 R_s pre-protocol; 2) R_s during any of the recorded protocols could not exceed 30 MΩ; 3) the offset
628 drift by the end of the recordings could not be higher than ± 5 mV.

629 Spontaneous synaptic currents (sEPSC) were recorded in VC at V_h = -70 mV in a single,
630 continuous sweep for 10 to 15 min, low-pass filtered at 2 kHz with a Bessel filter and sampled at
631 10 kHz frequency.

632 To establish the spiking threshold, each neuron was current-clamped at V_h ~ -70 ± 3 mV and
633 subject to a ramp-shaped 200-0 pA current injection with a 1s duration. The spike threshold was
634 determined as the membrane potential at which the first fully developed action potential (AP) was
635 visible. Each ramp injection was repeated 10x, and the averaged threshold value is reported for
636 the neuron.

637 To establish the firing properties of recorded neurons, each neuron was current-clamped as
638 described previously and subjected to a square-shaped series of current injections with 25pA Δ
639 per step to a maximum of 0 pA, with each step of 1 s duration and inter-step interval (ISI) of 10 s.
640 If necessary, the holding current was corrected during the protocol to maintain V_h at ~ -70 ± 3 mV.

641 During analyses, only fully-formed APs that crossed the 0 mV threshold were included.

642 All data acquisition was performed using pCLAMP software (Molecular Devices, USA).

643

644 *5.4 Field potential recordings – analyses.*

645 During field potential recordings, the biologically relevant signals are superimposed onto the
646 decaying stimulation artifact. To isolate the stimulation artifacts for subtraction from the signal at
647 the end of each recording, we applied 1 μM TTX to the slice and recorded 30 repetitions of each
648 stimulation paradigm were recorded in the presence of TTX.

649 Recorded traces were analyzed in IgorPro (Wavemetrics, USA). First, an average of the traces
650 recorded with TTX was subtracted from each trace. The traces were then filtered using a rolling
651 five-point average to remove noise, and the baseline was adjusted to the 1 s period before the
652 stimuli. The amplitudes and latencies of FVs and fEPSPs were measured at their peaks.
653 Amplitudes were measured against 0 mV baselines, while latencies were measured against the
654 onset of the stimulation. During high-frequency stimulation, cells often do not have sufficient time
655 to fully recover their membrane potentials before the next stimulus is applied, leading to a gradual
656 shift in the baseline, therefore, as a correction, we subtracted the median voltage at +35 to +40
657 ms after each stimulus from each FV or fEPSP amplitude. FV widths were measured at the peaks
658 of positive deflections in the waveform, first after the artifact subtraction and second directly before
659 fEPSP.

660 All traces were screened for occasional electrical interference and the affected data points were
661 manually removed from the analysis.

662 To measure axonal conduction velocity (CV), we calculated the time shift (Δt, ms) between the
663 stimulus start and the time of the FV peak. Next, the linear distance between the recording site
664 and the stimulation electrode was divided by the measured Δt. We recorded CV at 3-6 sites over
665 a span of 300-900 μm, with ~1 μm steps between sites. Each CV recording site served as a
666 replicate for statistical analysis (see Statistics). During CV recording, stimulation remained
667 stationary, and the sites were recorded in randomized order.

668 To calculate changes in FV peak latency during train stimulations the median Δt at stimulus 1-3
669 of traces 1-2 (Δt_N) was subtracted from each Δt (normalization).

670

671 *5.5 Field potential recordings – data visualization.*

672 For constructing "heatmap" visualizations of the data, numerical matrices of FV or fEPSP
673 amplitude means were built for each of the four treatment groups. In every matrix each new row

674 represented responses during each subsequent train. Then, two additional columns were added
675 at the end as a color normalization in the heatmap (0, 1 mV), and the matrix was saved as a text
676 file. Afterwards, the text files were imported as text images to ImageJ (NIH, USA), converted from
677 32- to 16-bit, saved as TIFF images and imported to IgorPro (Wavemetrics, USA), whereupon
678 their look-up table (LUT) was changed from "Grays" to "Spectrum."

679 The heat maps for latency changes during train stimulation were generated similarly but using
680 different normalizations: 20 pulse train recordings had normalization boundaries of -1 and +1 ms.

681

682 *5.6 Whole-cell patch-clamp – sEPSC analyses.*

683 sEPSCs detection was automatized using a convolution-based algorithm in Fbrain 3.03 [64], a
684 customized program running under IgorPro 6 (WaveMetrics, Lake Oswego, USA), kindly provided
685 by the Peter Jonas Lab (IST, Klosterneuburg, Austria). Recorded traces were smoothed by
686 subtracting a 20-term polynomial fitted to the trace and digital Notch (60 ± 0.5 Hz) filtered in FBrain
687 before the analysis. The trace subject to convolution was passed through a digital band-pass filter
688 at 0.001 to 200 Hz. The event detection template had a rise-time time constant τ = 1.5 ms, a
689 decay τ = 6 ms, and an amplitude of −10 pA. The event detection threshold (θ) was set to 4.2
690 times the standard deviation of a Gaussian function fitted to the all-point histogram of the
691 convolved trace. All events detected by the algorithm were inspected visually. Those that clearly
692 did not show fast rise time and exponential decay kinetics of a typical hippocampal EPSC were
693 removed by hand. Only cells with a rejection ratio lower than 20% were included in the analysis.
694 The analysis was performed using custom-written macros provided by Dr. Maria Kukley
695 (Achucarro Basque Center for Neuroscience, Bilbao, Spain).

696 Afterwards, individual sEPSC waveforms were extracted from the trace. Each waveform
697 consisted of a 5 ms segment of the trace before the onset of the sEPSC and a 50 ms piece after
698 the onset to capture the full decay of the waveform. Before averaging, all sEPSCs were baseline-
699 adjusted to the pre-onset 5 ms. The peak amplitude, 20-80% onset-to-peak rise time, and decay
700 constant τ were measured for the averaged sEPSC. The decay τ was calculated from the
701 monoexponential fit from the sEPSC peak to the final ms of the averaged waveform.

702 To avoid selection bias during sEPSC extraction, we repeated the Fbrain analysis at least twice
703 in each cell and averaged the results.

704

705 5.7 *Statistics.*

706 All data acquisitions were made in randomized sequence, with a maximum of 2 slices (field
707 potential recordings) or 2 cells (patch clamp recordings) from a single animal per experimental
708 condition to avoid pseudoreplication. All experimental groups had comparable distributions of

ages (close to P50 ± 6) and sex. The order of slice pre-incubation with drugs was randomized for each animal. The numbers of slices or cells and animals used in each experiment are indicated in the figure legends.

Statistical analysis was performed using GraphPad Prism 9.5.1 (GraphPad Software, USA). Significant outliers were removed with the Prism ROUT method at Q = 5%, and the normality of residuals and homoscedasticity were tested for each comparison. If the datasets had normal residuals and equal variances, we used ordinary one-way ANOVA with *post hoc* Holm-Šídák's test. If the datasets had normal residuals but unequal variances, we used Brown-Forsythe ANOVA with *post hoc* Dunnett's T3 test. If the datasets were not normally distributed but had equal variances, we used Kruskal-Wallis ANOVA with *post hoc* Dunn's test. In rare cases where the data was neither normally distributed nor had equal variance, we applied the Brown-Forsythe ANOVA with *post hoc* Dunnett's T3 test. If the dataset consisted of multiple replicates, we used nested one-way ANOVA with *post hoc* Holm-Šídák's test. The tested groups and p values are indicated in the text or the figure legends. Individual cells or slices are labeled as n, replicates are labeled as m, and the numbers animals used are labeled as N. If the groups tested as being different, we report the p-values of *post hoc* tests but omit the p-value of the omnibus test. If the groups did not test as different, only the p-value of an omnibus test is reported. For scatter plots, each point represents an individual data point (cell, slice, or replicate) and the horizontal bars represent the group mean ± SEM. In all other graphs, we present mean ± SEM. The heat maps represent the group means.

5.8 Model of conduction velocity

Here we model how AP shape affects the conduction velocity (CV) along an unmyelinated axon. We model an infinitesimally small unit of the axon consisting of three distinct units in a row, separated by a space h. The first and last of these units are kept "fixed" at voltages $V_1 = V_a$ (the peak membrane potential) and $V_3 = V_{rest}$, respectively; this potential difference leads to a voltage flow across the axon which is generally described by the cable equation [65]:

$$\lambda^2 \frac{\partial^2 V}{\partial x^2} = \tau \frac{\partial V}{\partial t} + V$$

Once the intermediate unit V_2 is excited above a threshold voltage V_t, the unit activates and is self-excited up to a voltage V_a. This process then repeats *ad infinitum* along the entirety of the axon (assuming no backflow of the charge). The conduction velocity (i.e., the rate of this voltage flow) is thus inversely proportional to the reset time t_{reset} (the first time when $V_2(t) = V_t$, with $V_2(0) = V_{rest}$ as well). Over the discrete lattice above, the cable equation is given by:

$$\lambda^2 \frac{V_3 - 2V_2 + V_1}{h^2} - \tau \frac{dV_2}{dt} = V_2$$

Solving this for $V_2(t)$ and substituting in the boundary conditions, we find:

$$V_2(t) = \frac{\lambda^2(V_{rest} + V_a)}{h^2 + 2\lambda^2} + Ke^{\frac{-1}{\tau}\left(1+\frac{2\lambda^2}{h^2}\right)t} = V_B + Ke^{\frac{-1}{\tau}\left(1+\frac{2\lambda^2}{h^2}\right)t}$$

where K is an integration constant needed to satisfy the initial condition $V_2(0) = V_{rest}$. Substituting in the initial condition and solving for t_{reset}, we find:

$$t_{reset} = \frac{-\tau}{1+\frac{2\lambda^2}{h^2}} log \frac{V_t - V_B}{V_{rest} - V_B}$$

Thus:

$$CV \propto \frac{1}{log \frac{V_{rest} - V_B}{V_t - V_B}}$$

However, h is an arbitrarily small spacing that we can take to approach zero. Thus:

$$CV \propto \frac{1}{log \frac{V_{rest} - V_a}{2V_t - V_{rest} - V_a}}$$

5.9 *Power and sample size calculations.*

The sample sizes for all statistical comparisons in this work were determined based on the means and pooled standard deviations from preliminary recordings of 8-10 cells or slices per group, α = 0.05, β = 0.8, corrected for the number of pairwise comparisons (τ), based on the following equations:

$$n = 2\left(\sigma \frac{z_{1-\alpha/(2\tau)} z_{1-\beta}}{\mu A - \mu B}\right)^2,$$

$$1 - \beta = \phi\left(z - z_{1-\alpha/(2\tau)}\right) + \phi\left(-z - z_{1-\alpha/(2\tau)}\right),$$

$$z = \frac{\mu A - \mu B}{\sigma\sqrt{\frac{2}{n}}},$$

Where n is the sample size, σ is standard deviation, ϕ is standard normal distribution function, α is Type I error rate, τ is the number of pairwise comparisons, and β is Type II error rate. During the calculations, the normality of residuals and equality of variances were assumed *a priori*.

All of the calculations were performed in an online calculator available at:

http://powerandsamplesize.com/Calculators/Compare-k-Means/1-Way-ANOVA-Pairwise

6. **References**

1. de la Monte SM. Insulin Resistance and Neurodegeneration: Progress Towards the Development of New Therapeutics for Alzheimer's Disease. Drugs. 2017;77(1):47-65. doi:10.1007/s40265-016-0674-0

2. De Felice FG, Ferreira ST. Inflammation, defective insulin signaling, and mitochondrial dysfunction as common molecular denominators connecting type 2 diabetes to Alzheimer disease. Diabetes. 2014;63(7):2262-2272. doi:10.2337/db13-1954

3. McNay EC, Recknagel AK. Brain insulin signaling: a key component of cognitive processes and a potential basis for cognitive impairment in type 2 diabetes. Neurobiol Learn Mem. 2011;96(3):432-442. doi:10.1016/j.nlm.2011.08.005

4. Zhao WQ, Chen H, Quon MJ, Alkon DL. Insulin and the insulin receptor in experimental models of learning and memory. Eur J Pharmacol. 2004;490(1-3):71-81. doi:10.1016/j.ejphar.2004.02.045

5. McNay EC, Recknagel AK. Brain insulin signaling: a key component of cognitive processes and a potential basis for cognitive impairment in type 2 diabetes. Neurobiol Learn Mem. 2011;96(3):432-442. doi:10.1016/j.nlm.2011.08.005

6. Ghasemi R, Haeri A, Dargahi L, Mohamed Z, Ahmadiani A. Insulin in the brain: sources, localization and functions. Mol Neurobiol. 2013;47(1):145-171. doi:10.1007/s12035-012-8339-9

7. Kuwabara T, Kagalwala MN, Onuma Y, et al. Insulin biosynthesis in neuronal progenitors derived from adult hippocampus and the olfactory bulb. EMBO Mol Med. 2011;3(12):742-754. doi:10.1002/emmm.201100177

8. McNay EC, Pearson-Leary J. GluT4: A central player in hippocampal memory and brain insulin resistance. Exp Neurol. 2020;323:113076. doi:10.1016/j.expneurol.2019.113076

9. Craft S. Insulin resistance syndrome and Alzheimer's disease: age- and obesity-related effects on memory, amyloid, and inflammation. Neurobiol Aging. 2005;26 Suppl 1:65-69. doi:10.1016/j.neurobiolaging.2005.08.021

10. Kerti L, Witte AV, Winkler A, Grittner U, Rujescu D, Flöel A. Higher glucose levels associated with lower memory and reduced hippocampal microstructure. Neurology. 2013;81(20):1746-1752. doi:10.1212/01.wnl.0000435561.00234.ee

11. Antal B, McMahon LP, Sultan SF, et al. Type 2 diabetes mellitus accelerates brain aging and cognitive decline: Complementary findings from UK Biobank and meta-analyses. Elife. 2022;11:e73138. Published 2022 May 24. doi:10.7554/eLife.73138

12. McEwen BS, Reagan LP. Glucose transporter expression in the central nervous system: relationship to synaptic function. Eur J Pharmacol. 2004;490(1-3):13-24.

801 doi:10.1016/j.ejphar.2004.02.041

802 13. Pearson-Leary J, McNay EC. Novel Roles for the Insulin-Regulated Glucose Transporter-
803 4 in Hippocampally Dependent Memory. J Neurosci. 2016;36(47):11851-11864.
804 doi:10.1523/JNEUROSCI.1700-16.2016

805 14. McNay EC, Fries TM, Gold PE. Decreases in rat extracellular hippocampal glucose
806 concentration associated with cognitive demand during a spatial task. Proc Natl Acad Sci U S A.
807 2000;97(6):2881-2885. doi:10.1073/pnas.0583697

808 15. Grillo CA, Piroli GG, Hendry RM, Reagan LP. Insulin-stimulated translocation of GLUT4
809 to the plasma membrane in rat hippocampus is PI3-kinase dependent. Brain Res. 2009;1296:35-
810 45. doi:10.1016/j.brainres.2009.08.005

811 16. Stranahan AM, Norman ED, Lee K, et al. Diet-induced insulin resistance impairs
812 hippocampal synaptic plasticity and cognition in middle-aged rats. Hippocampus.
813 2008;18(11):1085-1088. doi:10.1002/hipo.20470

814 17. Ashrafi G, Wu Z, Farrell RJ, Ryan TA. GLUT4 Mobilization Supports Energetic Demands
815 of Active Synapses. Neuron. 2017;93(3):606-615.e3. doi:10.1016/j.neuron.2016.12.020

816 18. De Felice FG, Ferreira ST. Inflammation, defective insulin signaling, and mitochondrial
817 dysfunction as common molecular denominators connecting type 2 diabetes to Alzheimer
818 disease. Diabetes. 2014;63(7):2262-2272. doi:10.2337/db13-1954

819 19. Kothari V, Luo Y, Tornabene T, et al. High fat diet induces brain insulin resistance and
820 cognitive impairment in mice. Biochim Biophys Acta Mol Basis Dis. 2017;1863(2):499-8.
821 doi:10.1016/j.bbadis.2016.10.006

822 20. Martínez-François JR, Fernández-Agüera MC, Nathwani N, et al. BAD and KATP
823 channels regulate neuron excitability and epileptiform activity. Elife. 2018;7:e32721. Published
824 2018 Jan 25. doi:10.7554/eLife.32721

825 21. Kashiwaya Y, Takeshima T, Mori N, Nakashima K, Clarke K, Veech RL. D-beta-
826 hydroxybutyrate protects neurons in models of Alzheimer's and Parkinson's disease. Proc Natl
827 Acad Sci U S A. 2000;97(10):5440-5444. doi:10.1073/pnas.97.10.5440

828 22. Chikahisa S, Shimizu N, Shiuchi T, Séi H. Ketone body metabolism and sleep
829 homeostasis in mice. Neuropharmacology. 2014;79:399-404.
830 doi:10.1016/j.neuropharm.2013.12.009

831 23. Puchalska P, Crawford PA. Multi-dimensional Roles of Ketone Bodies in Fuel Metabolism,
832 Signaling, and Therapeutics. Cell Metab. 2017;25(2):262-284. doi:10.1016/j.cmet.2016.12.022

24. Ma W, Berg J, Yellen G. Ketogenic diet metabolites reduce firing in central neurons by opening K(ATP) channels. J Neurosci. 2007;27(14):3618-3625. doi:10.1523/JNEUROSCI.0132-07.2007

25. Jensen NJ, Wodschow HZ, Nilsson M, Rungby J. Effects of Ketone Bodies on Brain Metabolism and Function in Neurodegenerative Diseases. Int J Mol Sci. 2020;21(22):8767. Published 2020 Nov 20. doi:10.3390/ijms21228767

26. Hartman AL, Gasior M, Vining EP, Rogawski MA. The neuropharmacology of the ketogenic diet. Pediatr Neurol. 2007;36(5):281-292. doi:10.1016/j.pediatrneurol.2007.02.008

27. Xin L, Ipek Ö, Beaumont M, et al. Nutritional Ketosis Increases NAD+/NADH Ratio in Healthy Human Brain: An in Vivo Study by 31P-MRS. Front Nutr. 2018;5:62. Published 2018 Jul 12. doi:10.3389/fnut.2018.00062

28. Maalouf M, Sullivan PG, Davis L, Kim DY, Rho JM. Ketones inhibit mitochondrial production of reactive oxygen species production following glutamate excitotoxicity by increasing NADH oxidation. Neuroscience. 2007;145(1):256-264. doi:10.1016/j.neuroscience.2006.11.06

29. Shimazu T, Hirschey MD, Newman J, et al. Suppression of oxidative stress by β-hydroxybutyrate, an endogenous histone deacetylase inhibitor. Science. 2013;339(6116):211-214. doi:10.1126/science.1227166

30. Lutas A, Yellen G. The ketogenic diet: metabolic influences on brain excitability and epilepsy. Trends Neurosci. 2013;36(1):32-40. doi:10.1016/j.tins.2012.11.005

31. Clarke K, Tchabanenko K, Pawlosky R, et al. Kinetics, safety and tolerability of (R)-3-hydroxybutyl (R)-3-hydroxybutyrate in healthy adult subjects. Regul Toxicol Pharmacol. 2012;63(3):401-408. doi:10.1016/j.yrtph.2012.04.008

32. Kesl SL, Poff AM, Ward NP, et al. Effects of exogenous ketone supplementation on blood ketone, glucose, triglyceride, and lipoprotein levels in Sprague-Dawley rats. Nutr Metab (Lond). 2016;13:9. Published 2016 Feb 4. doi:10.1186/s12986-016-0069-y

33. Weistuch C, Mujica-Parodi LR, Razban RM, et al. Metabolism modulates network synchrony in the aging brain. Proc Natl Acad Sci U S A. 2021;118(40):e2025727118. doi:10.1073/pnas.2025727118

34. Mujica-Parodi LR, Amgalan A, Sultan SF, et al. Diet modulates brain network stability, a biomarker for brain aging, in young adults. Proc Natl Acad Sci U S A. 2020;117(11):6170-6177. doi:10.1073/pnas.1913042117

35. Hruz PW, Murata H, Qiu H, Mueckler M. Indinavir induces acute and reversible peripheral insulin resistance in rats. Diabetes. 2002;51(4):937-942. doi:10.2337/diabetes.51.4.937

866 36. Hresko RC, Hruz PW. HIV protease inhibitors act as competitive inhibitors of the
867 cytoplasmic glucose binding site of GLUTs with differing affinities for GLUT1 and GLUT4. PLoS
868 One. 2011;6(9):e25237. doi:10.1371/journal.pone.0025237

869 37. Colgin LL, Denninger T, Fyhn M, et al. Frequency of gamma oscillations routes flow of
870 information in the hippocampus. Nature. 2009;462(7271):353-357. doi:10.1038/nature08573

871 38. Buzsáki G, Wang XJ. Mechanisms of gamma oscillations. Annu Rev Neurosci.
872 2012;35:203-225. doi:10.1146/annurev-neuro-062111-1444

873 39. Catterall WA. From ionic currents to molecular mechanisms: the structure and function of
874 voltage-gated sodium channels. Neuron. 2000;26(1):13-25. doi:10.1016/s0896-6273(00)81133-2

875 40. Howarth C, Gleeson P, Attwell D. Updated energy budgets for neural computation in the
876 neocortex and cerebellum. J Cereb Blood Flow Metab. 2012;32(7):1222-1232.
877 doi:10.1038/jcbfm.2012.35

878 41. Lujan B, Kushmerick C, Banerjee TD, Dagda RK, Renden R. Glycolysis selectively shapes
879 the presynaptic action potential waveform. J Neurophysiol. 2016;116(6):2523-2540.
880 doi:10.1152/jn.00629.2016

881 42. Padamsey Z, Katsanevaki D, Dupuy N, Rochefort NL. Neocortex saves energy by
882 reducing coding precision during food scarcity. Neuron. 2022;110(2):280-296.e10.
883 doi:10.1016/j.neuron.2021.10.024

884 43. Jensen TP, Zheng K, Cole N, Marvin JS, Looger LL, Rusakov DA. Multiplex imaging
885 relates quantal glutamate release to presynaptic Ca2+ homeostasis at multiple synapses in situ.
886 Nat Commun. 2019;10(1):1414. Published 2019 Mar 29. doi:10.1038/s41467-019-09216-8

887 44. Newman JC, Verdin E. β-Hydroxybutyrate: A Signaling Metabolite. Annu Rev Nutr.
888 2017;37:51-76. doi:10.1146/annurev-nutr-071816-064916

889 45. Lund TM, Obel LF, Risa Ø, Sonnewald U. β-Hydroxybutyrate is the preferred substrate for
890 GABA and glutamate synthesis while glucose is indispensable during depolarization in cultured
891 GABAergic neurons. Neurochem Int. 2011;59(2):309-318. doi:10.1016/j.neuint.2011.06.002

892 46. Scott RS, Henneberger C, Padmashri R, Anders S, Jensen TP, Rusakov DA. Neuronal
893 adaptation involves rapid expansion of the action potential initiation site. *Nat Commun*.
894 2014;5:3817. Published 2014 May 23. doi:10.1038/ncomms4817

895 47. Stranahan AM, Mattson MP. Impact of energy intake and expenditure on neuronal
896 plasticity. Neuromolecular Med. 2008;10(4):209-218. doi:10.1007/s12017-008-8043-0

897 48. Piroli GG, Grillo CA, Reznikov LR, et al. Corticosterone impairs insulin-stimulated

898 translocation of GLUT4 in the rat hippocampus. Neuroendocrinology. 2007;85(2):71-80.
899 doi:10.1159/000101694

900 49. Grillo CA, Piroli GG, Hendry RM, Reagan LP. Insulin-stimulated translocation of GLUT4
901 to the plasma membrane in rat hippocampus is PI3-kinase dependent. Brain Res. 2009;1296:35-
902 45. doi:10.1016/j.brainres.2009.08.005

903 50. Leloup C, Arluison M, Kassis N, et al. Discrete brain areas express the insulin-responsive
904 glucose transporter GLUT4. Brain Res Mol Brain Res. 1996;38(1):45-53. doi:10.1016/0169-
905 328x(95)00306-d

906 51. Vannucci SJ, Koehler-Stec EM, Li K, Reynolds TH, Clark R, Simpson IA. GLUT4 glucose
907 transporter expression in rodent brain: effect of diabetes. Brain Res. 1998;797(1):1-11.
908 doi:10.1016/s0006-8993(98)00103-6

909 52. 42. Miranda M, Morici JF, Zanoni MB, Bekinschtein P. Brain-Derived Neurotrophic Factor:
910 A Key Molecule for Memory in the Healthy and the Pathological Brain. Front Cell Neurosci.
911 2019;13:363. Published 2019 Aug 7. doi:10.3389/fncel.2019.00363

912 53. Won SJ, Yoo BH, Kauppinen TM, et al. Recurrent/moderate hypoglycemia induces
913 hippocampal dendritic injury, microglial activation, and cognitive impairment in diabetic rats. J
914 Neuroinflammation. 2012;9:182. Published 2012 Jul 25. doi:10.1186/1742-2094-9-182

915 54. 44. Yamada KA, Rensing N, Izumi Y, et al. Repetitive hypoglycemia in young rats impairs
916 hippocampal long-term potentiation. Pediatr Res. 2004;55(3):372-379.
917 doi:10.1203/01.PDR.0000110523.07240.C

918 55. Lee SY, Kim JH. Mechanisms underlying presynaptic Ca2+ transient and vesicular
919 glutamate release at a CNS nerve terminal during in vitro ischaemia. J Physiol.
920 2015;593(13):2793-2806. doi:10.1113/JP270060

921 56. García-Rodríguez D, Giménez-Cassina A. Ketone Bodies in the Brain Beyond Fuel
922 Metabolism: From Excitability to Gene Expression and Cell Signaling. Front Mol Neurosci.
923 2021;14:732120. Published 2021 Aug 27. doi:10.3389/fnmol.2021.732120
924
925 57. van Nieuwenhuizen, H., Chesebro, A. G., Polizu, C., Clarke, K., Strey, H. H., Weistuch,
926 C., & Mujica-Parodi, L. R. Ketosis regulates K+ ion channels, strengthening brain-wide signaling
927 disrupted by age. *bioRxiv*, 2023-05.

928 58. Ma W, Berg J, Yellen G. Ketogenic diet metabolites reduce firing in central neurons by
929 opening K(ATP) channels. J Neurosci. 2007;27(14):3618-3625. doi:10.1523/JNEUROSCI.0132-
930 07.2007

931 59. Tanner GR, Lutas A, Martínez-François JR, Yellen G. Single K ATP channel opening in

response to action potential firing in mouse dentate granule neurons. J Neurosci. 2011;31(23):8689-8696. doi:10.1523/JNEUROSCI.5951-10.2011

60. Martínez-François JR, Fernández-Agüera MC, Nathwani N, et al. BAD and KATP channels regulate neuron excitability and epileptiform activity. Elife. 2018;7:e32721. Published 2018 Jan 25. doi:10.7554/eLife.32721

61. Lund TM, Ploug KB, Iversen A, Jensen AA, Jansen-Olesen I. The metabolic impact of β-hydroxybutyrate on neurotransmission: Reduced glycolysis mediates changes in calcium responses and KATP channel receptor sensitivity. J Neurochem. 2015;132(5):520-531. doi:10.1111/jnc.12975

62. Fremeau RT Jr, Kam K, Qureshi T, et al. Vesicular glutamate transporters 1 and 2 target to functionally distinct synaptic release sites. Science. 2004;304(5678):1815-1819. doi:10.1126/science.1097468

63. Juge N, Gray JA, Omote H, et al. Metabolic control of vesicular glutamate transport and release. Neuron. 2010;68(1):99-112. doi:10.1016/j.neuron.2010.09.002

64. Pernía-Andrade AJ, Goswami SP, Stickler Y, Fröbe U, Schlögl A, Jonas P. A deconvolution-based method with high sensitivity and temporal resolution for detection of spontaneous synaptic currents in vitro and in vivo. Biophys J. 2012;103(7):1429-1439. doi:10.1016/j.bpj.2012.08.039

65. Koch C, Chapter 6: The Hodgkin and Huxley Model of Action Potential Generation. In: Koch C, Biophysics of Computation: Information Processing in Single Neurons. Oxford University Press. 2004. p. 139-176. Print.

66. Traub RD, Wong RK, Miles R, Michelson H. A model of a CA3 hippocampal pyramidal neuron incorporating voltage-clamp data on intrinsic conductances. J Neurophysiol. 1991;66(2):635-6. doi:10.1152/jn.1991.66.2.635

67. Yu N, Morris CE, Joós B, Longtin A. Spontaneous excitation patterns computed for axons with injury-like impairments of sodium channels and Na/K pumps. PLoS Comput Biol. 2012;8(9):e1002664. doi:10.1371/journal.pcbi.1002664

68. Altemus KL, Lavenex P, Ishizuka N, Amaral DG. Morphological characteristics and electrophysiological properties of CA1 pyramidal neurons in macaque monkeys. Neuroscience. 2005;136(3):741-756. doi:10.1016/j.neuroscience.2005.07.001

7. **Acknowledgments**

We thank Dr. Vittorio Gallo (Children's National Research Institute, USA) for sharing his electrophysiology setup, without which this work would not have been possible; Dr. Kieran Clarke (University of Oxford) for providing D-βHb ester and advice; Dr. Joseph Abbah (Children's National Research Institute, USA) for help during the preliminary stage of the research; Dr. Richard L. Veech and Dr. M. Todd King (Lab of Metabolic Control, NIH/NIAAA, USA) for providing D-βHb ester and advice; Dr. Ting-Jiun Chen (Mt. Sinai Medical Center, USA) for help and advice with setting up patch clamp recordings; Dr. Peter Jonas (Institute of Science and Technology Austria, Austria) for providing FBrain software; Dr Fernando Fernandez (Boston University, USA) for comments to the first draft of the manuscript; Dr Paul Hruz (Washington University School of Medicine in St. Louis, USA) for help with establishing the GluT4 inhibition model; Dr Nandkishore Prakash and Dave Saxon (Children's National Research Institute, USA) for advice and discussions; Dr Heidi Matos Galicia (National Institute of Neurological Disorders and Stroke, USA) for advice; Dr. Paul Cumming (Bern University Hospital) for critical reading of the manuscript; and members of the Mujica-Parodi laboratory (LCNeuro, USA) for discussions; C.W. also acknowledges support from the Marie-Josée Kravis Fellowship in Quantitative Biology.

8. **Funding**

This work was supported by the National Institutes of Health Grant K01NS110981 to N.A.S., the National Science Foundation NSF1926781 to L.M.P. and N.A.S., and the Department of Defense ARO W91NF2010189 to N.A.S.

9. **Contributions**

Conceptualization: BK, BA, CW, LMP, NAS

Methodology: BK, BA, FG, AB, JMH, CW, MK, LMP, NAS

Software: FG, AB, JMH, BA, CW, MK

Validation: BK, BA, CW, LMP, NAS

Formal Analysis: BK, BA, CW, FG, AB, JMH

Investigation: BK, BA, CW, FG, AB, JMH, LMP, NAS

Writing – Original Draft: BK

Writing – Review & Editing: BK, BA, CW, FG, AB, VV, JMH, MK, LMP, NAS

Visualization: BK, BA

Supervision: LMP, NAS

Funding Acquisition: LMP, NAS

10. **Competing Interests**

Authors declare no competing interest.

11. **Data and materials availability**

Raw data presented in this work, data tables with analyses and tables with statistics are available upon request. All code is available on GitHub, by following the links provided in the text.

12. **Supplementary materials**

Figures S1 to S8, Supplementary Methods.